The Astronomical Journal, 129:104–124, 2005 January

JET-GAS INTERACTION IN MARKARIAN 78. II. IONIZATION MECHANISMS

M. Whittle,[1] D. J. Rosario,[1] J. D. Silverman,[1,2] C. H. Nelson,[3] and A. S. Wilson[4,5]

Received 2004 July 19; accepted 2004 October 5

ABSTRACT

We investigate the ionization mechanisms in the Seyfert galaxy Markarian 78, chosen because its narrow-line region (NLR) is dominated by a strong jet-gas interaction. Our principal aim is to ascertain whether or not shock-related ionization is important. We use *Hubble Space Telescope* (*HST*) Space Telescope Imaging Spectrograph (STIS) optical and UV spectra from four slits, as well as *HST* Faint Object Spectrograph optical spectra from 10 apertures. Ultimately, several lines of evidence argue *against* the importance of shocks but *in favor* of central source photoionization, even for gas that is clearly accelerated by the jet flow.

Following earlier work, we compare emission-line ratios with four classes of ionization model: photoionization of optically thick gas (standard and dusty U sequences), photoionization of optically thick and thin gas ($A_{m/i}$ sequence), and fast shocks. Traditional excitation measures are well matched by all three models, with $-3.0 < \log U < -2.0$, $-0.5 < \log A_{m/i} < +1.0$, and 300 km s^{-1} $< V_{\rm shock} <$ 500 km s^{-1}. However, several other line ratios provide clear discrimination, with significantly poorer fits for standard and dusty U models and even poorer for shock models. Importantly, our data span a sufficient range of conditions that they show *trends* in the ratio-ratio plots, and these trends clearly favor central source photoionization models, particularly the $A_{m/i}$ models. To achieve essentially perfect agreement, we make two slight modifications to the $A_{m/i}$ models of Binette et al.: we lower the ionization of the optically thin component (Mrk 78 has somewhat lower than normal excitation), and we increase the nitrogen abundance toward the nucleus. We suspect that this latter effect has introduced ambiguities in previous work. The UV lines are less helpful than anticipated, partly because of their weakness and partly because high ionization parameter photoionization can mimic shocks. An exception is N v, which, in the absence of abundance effects, can provide unambiguous discrimination.

We extend the above analysis to include comparison of line profiles. We first show that even slight differences in velocity between pre- and postshock gas (shock scenario) and optically thin and thick gas ($A_{m/i}$ scenario) predict significant profile differences between [O iii] λ5007 and other emission lines. The marked *absence* of such differences argues strongly against the two-component shock models and also demands, for an $A_{m/i}$ model, that optically thin and thick gas have similar velocity distributions. The possible presence, however, of a weak broad low-ionization component may indicate a minor shock contribution. Further evidence against shock ionization is the absence of correlations between line ratios and kinematic parameters (e.g., FWHM or $V_{\rm peak}$); that is, the calmest and the most turbulent gas both have similar ionization. Conversely, a global decrease in excitation away from the nucleus qualitatively supports central source photoionization. Quantitatively, however, Mrk 78 exhibits the so-called Q problem seen in many other active galactic nuclei, although we speculate that a detailed extension of $A_{m/i}$-type models may resolve the problem without requiring in situ sources of ionization. Finally, we use NLR excitation and far-infrared luminosity to provide two independent estimates of the nuclear ionizing luminosity. Both these estimates match the simple picture of central source photoionization, yielding the observed emission-line luminosity and a plausible ($\sim$20%–100%) NLR covering factor.

We conclude that despite the NLR in Mrk 78 being strongly disturbed by radio-emitting ejecta, there is little or no evidence for shock-related ionization. There is, however, strong evidence for central source photoionization, including both optically thick and thin gaseous components. In Paper III we make further use of the STIS data to derive the dynamics of the emission-line region and the nature of the jet flow.

Key words: galaxies: individual (Markarian 78) — galaxies: jets — galaxies: kinematics and dynamics — galaxies: Seyfert — ISM: jets and outflows

1. INTRODUCTION

This is the second of three papers that present a detailed study of the Seyfert galaxy Markarian 78. We chose Mrk 78 because it presents one of the clearest examples of the interaction between bipolar radio-emitting ejecta and a kiloparsec-scale emission-line region, and our overall aim is to understand the physical processes inherent to this interaction. Such interactions are common in active galactic nuclei (AGNs), and so we hope that our study of Mrk 78 will give insight into the wider phenomena of jet-disturbed emission-line regions. In Paper I (Whittle & Wilson 2004) we constructed a qualitative picture of the jet-gas interaction, drawing upon emission-line, continuum, and radio images, as well as limited spectroscopy. In this paper, we introduce more extensive spectroscopy and use it to identify the dominant ionization mechanisms affecting the emission-line gas. In Paper III (Whittle et al. 2004) we use

[1] Department of Astronomy, University of Virginia, Charlottesville, VA 22903; dmw8f@virginia.edu, djr4t@virginia.edu, jds6h@virginia.edu.
[2] Current address: Max Planck Institute for Extraterrestrial Physics, Giessenbachstrasse, 85748 Garching, Germany.
[3] Department of Physics and Astronomy, Drake University, Des Moines, IA 50311-4505; charles.nelson@drake.edu.
[4] Department of Astronomy, University of Maryland, College Park, MD 20742; wilson@astro.umd.edu.
[5] Adjunct Astronomer, Space Telescope Science Institute.

this same data set to study the dynamics of the gas and from this deduce the nature of the radio-emitting bipolar flow.

The overall context and background to this study are given in the introduction to Paper I. Here we briefly review the motivation for investigating the ionization mechanism of the kiloparsec-scale emission-line region in Mrk 78 (the narrow-line region [NLR]). It might seem odd to embark on such a study given the general acceptance of central source photoionization over the past 30 years, but recently a number of developments have brought the question of NLR ionization in AGNs back to center stage. The original evidence for photoionization was, of course, the remarkably tight correlation between nonstellar continuum and Balmer line luminosities (Yee 1980; Shuder 1981) and the general success of models with power-law continua photoionizing optically thick clouds (e.g., Davidson & Netzer 1979). The situation began to look more complicated in the early 1980s when VLA radio images revealed collimated nuclear radio ejecta that terminated, and hence deposited their energy, within the NLRs of many Seyfert galaxies (Wilson & Willis 1980). Furthermore, collisional ionization by shocks was invoked to explain the low-ionization (supernova remnant–like) spectra of LINERs (e.g., Fosbury et al. 1978; Heckman 1980), although further work suggested that LINER spectra might represent photoionization of gas at a low ionization parameter (e.g., Ferland & Netzer 1983; Halpern & Steiner 1983). Indications that simple photoionization models were genuinely lacking became clearer in the late 1980s with more detailed studies, particularly of extended emission. First, the models systematically underpredict some of the weaker but important lines, such as [O III] λ4363 (creating the "[O III] temperature problem") and the high-ionization lines such as [Ne V] λ3426 and [Fe VII] λ6087. Second, gradients in excitation and gas density (estimated from the [S II] lines) are often inconsistent with simple r^{-2} dilution of a central radiation field. In the mid-1990s these and other difficulties motivated further theoretical work that developed along two lines: extending the photoionization picture to include optically thin gas (e.g., Binette et al. 1996, hereafter BWS96) and pushing shock models to higher velocities, at which the post-shock region becomes a strong source of ionizing photons (e.g., Dopita & Sutherland 1995, 1996; hereafter DS95, DS96). Interestingly, these new fast-shock models yield sufficiently high ionization that they become a possible contender for *all* extended AGN emission-line regions, not just those with weak nuclear UV sources or those with strong jet-gas interactions (e.g., Sutherland et al. 1993; DS95). In the past few years, this suite of old and new ionization models has been applied in a variety of contexts with the hope of establishing which, if any, is the more nearly correct. It is probably fair to say that at the present time, although individual studies may favor one or other ionization scenario, no clear-cut answer has yet emerged.

Our contribution to this ongoing debate is to take the following approach: we choose to study an object in which the NLR exhibits such high jet-driven velocities that shock models should have their greatest chance of success. If we find no evidence of shock-related ionization in this object, it casts serious doubt on the importance of shocks, certainly in related objects, and possibly in general.

In §§ 2 and 3 we introduce the observations and their measurements, including line fluxes and [O III] λ5007 profile kinematics. In § 4 we review the various ionization models, which in § 5 we compare with the data using a wide range of line ratio-ratio diagrams. We extend this analysis in § 6 to include comparison of profile shapes, and in § 7 we make a more direct test of shock models by looking for correlations between line ratios and kinematic parameters. In § 7 we also discuss the presence of a radial gradient in excitation, and in § 8 we apply and confirm two simple tests of the central source photoionization scenario. We briefly note in § 9 some recent related results coming from X-ray spectroscopy before summarizing our conclusions in § 10.

2. OBSERVATIONS

Mrk 78 was observed using the *Hubble Space Telescope* Space Telescope Imaging Spectrograph (*HST* STIS; Kimble et al. 1998; Woodgate et al. 1998) using four gratings (G140L, G430L, G430M, and G750M) at each of four slit locations (see Table 1 for details). Figure 1 shows the slit locations superposed on the PC [O III] emission-line image taken from Paper I: three slits lie parallel to the radio axis (slits A, B, and C; P.A. = 88°.0), and a fourth diagonal slit crosses the brightest emission regions and includes the highly reddened nucleus (slit D; P.A. = 61°.5). Overall, the slits cover essentially all major emission-line features. The four gratings provide full optical-UV coverage at intermediate resolution, allowing an ionization study (this paper), as well as high resolution in the red and green, allowing a dynamical study (Paper III).

In addition to these spectroscopic observations, we also took a number of direct images using STIS, as well as a slitless image using the G430M grating (see Table 2 for details). The direct images were used to assist in subsequent spectroscopic target acquisition and to provide additional information on the continuum morphology. The dispersed slitless image was taken to assess the potential for future use of such images and is discussed further in Paper III.

We also draw upon data presented in Paper I, which includes a high signal-to-noise ratio (S/N) [O III] Planetary Camera (PC) image, a deep 3.6 cm VLA radio image, several lower S/N PC and Faint Object Camera (FOC) continuum images, a NICMOS image, and Faint Object Spectrograph (FOS) spectra taken through 10 apertures (also shown in Fig. 1). See Tables 1 and 2 of Paper I for details of these observations. The naming system of NLR features, such as the inner and outer eastern fan, western lobe, and western knot and the regions LW-1, LE-1, etc., are presented in Figure 4 of Paper I.

3. REDUCTION AND MEASUREMENTS

3.1. *Data Preparation*

The STIS data were calibrated within CALSTIS. For the CCD data, remaining cosmic rays and hot pixels were removed within IRAF using the task COSMICRAYS. The slit locations were verified by comparing the [O III] λ5007 flux distribution along each slit with the [O III] flux distribution taken from slices across the PC image. The optimum match agrees with the positions specified for the spacecraft acquisition (and shown in our figures) to within $\sim$0.5 STIS pixels ($\sim$0″.02).

Continuum subtraction can be important when measuring weak lines, particularly in the blue. For this reason most care was taken for the G430L spectra in the range 3200–5700 Å. Guided by a high-S/N ground-based spectrum, we established an initial stellar population mix, which was then optimized within each slit region. Optimization involved a simple minimum χ^2 fit to a template, using only regions between emission lines, each region weighted according to its S/N and importance for the subtraction. Included in our template library were galaxy spectra from González Delgado et al. (2001), Starburst99 model spectra (Leitherer et al. 1999), Balmer

TABLE 1
HST STIS Spectroscopic Observations

Property	G140L λ = 1123–1719 Å $\Delta\lambda$ = 0.583 Å pixel^{-1} Δcz = 144 (at Lyα)	G430L λ = 2900–5700 Å $\Delta\lambda$ = 2.75 Å pixel^{-1} Δcz = 165 (at λ5007)	G430M λ = 4950–5236 Å $\Delta\lambda$ = 0.277 Å pixel^{-1} Δcz = 17 (at λ5007)	G750M λ = 6480–7054 Å $\Delta\lambda$ = 0.555 Å pixel^{-1} Δcz = 25 (at Hα)
Slit A:				
Data set	O4DJ03010	O4DJ02030	O4DJ02020	O4DJ02010
Date (visit)	1998 Mar 25 (3)	1998 Feb 28 (2)	1998 Feb 28 (2)	1998 Feb 28 (2)
Exposure time (s)	1750	2052	1727	1100
Offset (arcsec)	(0.125, 0.0)	(0.125, 0.0)	(0.125, 0.0)	(0.125, 0.0)
Slit B:				
Data set	O4DJ03020, 03030	O4DJ02060	O4DJ02050	04DJ02040
Date (visit)	1998 Mar 25 (3)	1998 Feb 28 (2)	1998 Feb 28 (2)	1998 Feb 28 (2)
Exposure time (s)	610, 1200	1730	1938	1199
Offset (arcsec)	(0.27, 0.0)	(0.27, 0.30)	(0.27, 0.0)	(0.27, 0.0)
Slit C:				
Data set	O4DJ03040	O4DJ02090	O4DJ02080	O4DJ02070
Date (visit)	1998 Mar 25 (3)	1998 Mar 1 (4)	1998 Feb 28 (2)	1998 Feb 28 (2)
Exposure time (s)	1671	2052	2052	1172
Offset (arcsec)	(−0.55, 0.0)	(−0.55, 0.0)	(−0.55, 0.0)	(−0.55, 0.0)
Slit D:				
Data set	O4DJ55020	O4DJ04010	O4DJ04020	O4DJ0430
Date (visit)	1998 Oct 12 (5)	1998 Mar 1 (4)	1998 Mar 1 (4)	1998 Mar 1 (4)
Exposure time (s)	1377	1643	1800	1320
Offset (arcsec)	(0.05, 0.0)	(−0.05, 0.0)	(−0.05, 0.0)	(−0.05, 0.0)

Notes.—For all observations, the aperture was set at $52'' \times 0''.2$. Position angle was set equal to $88^{\circ}.056$, except for the observations with slit D, for which it was $61^{\circ}.556$ for the G430L, G430M, and G750M filters and $-118^{\circ}.50$ for G140L. Units of Δcz are km s^{-1} pixel^{-1}.

continuum emission (constrained to match the Hβ flux), and reddening. In practice, the population mix stayed close to a 3:1 ratio of intermediate (700 Myr) and old (10–15 Gyr) populations, which is consistent with the mix found for Mrk 78 by González Delgado et al. (2001). What does vary along the slit is the reddening required to get the overall spectral shape. These reddening estimates do, in fact, follow reasonably closely the estimates made using the Hα/Hβ ratio. Following the warnings of Keel & Miller (1983), Storchi-Bergmann et al. (1996b), and Filippenko & Halpern (1984), we paid particular attention to the G-band region, since the measured line strengths for [O III] λ4363 and Hγ are very sensitive to the exact shape of the

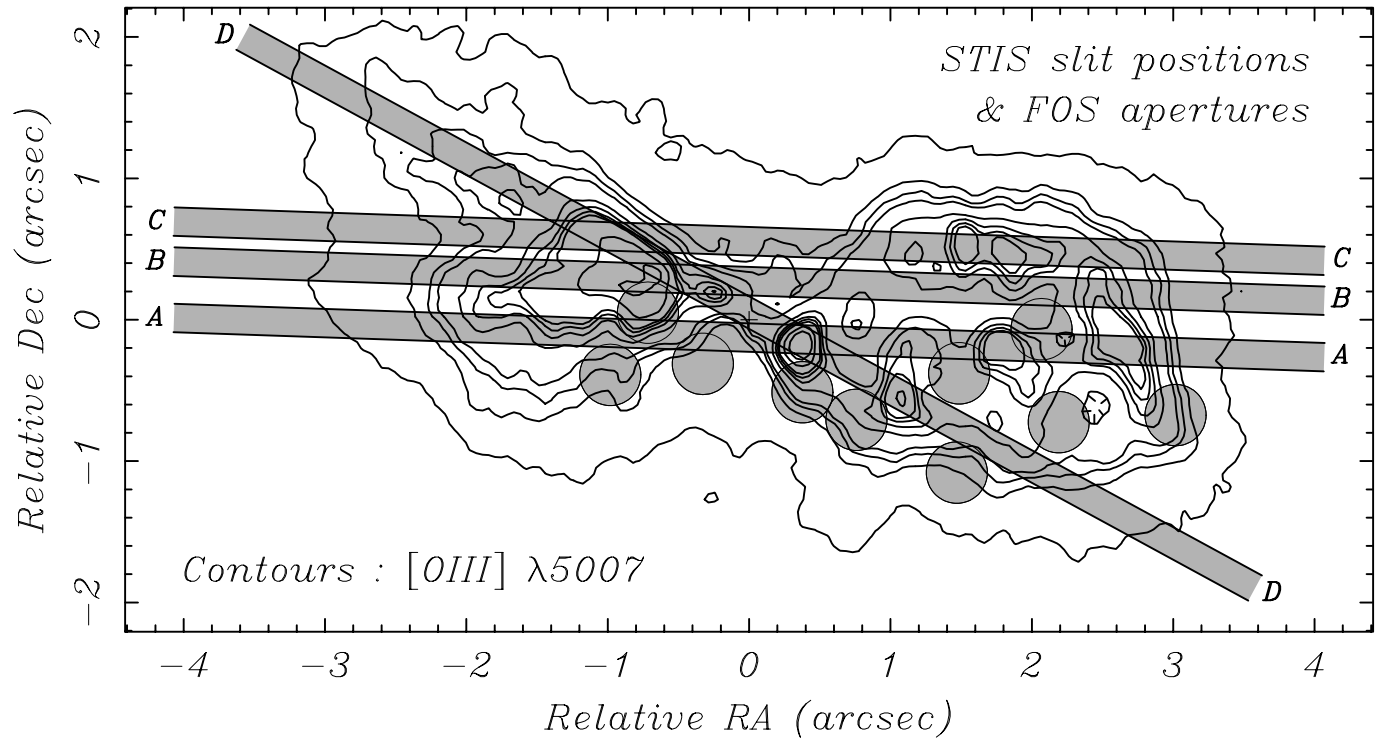

Fig. 1.—STIS slit and FOS circular aperture locations shown superposed on a contour plot of the [O III] $\lambda\lambda$4959, 5007 PC image taken from Paper I.

TABLE 2
HST STIS Imaging Observations

Data Set	Aperture	FOV (arcsec)	Grating	λ Range (Å)	Date (Visit)	Exposure (s)
O4DJ01010	F28X50LP-CCD	28 × 51	...	5500–11000	1997 Nov 16 (1)	240
O4DJ02M8S	F28X50LP-CCD	28 × 51	...	5500–11000	1998 Feb 28 (2)	20
O4DJ02NLQ	F28X50LP-CCD	28 × 51	...	5500–11000	1998 Feb 28 (2)	20
O4DJ04OLQ	F28X50LP-CCD	28 × 51	...	5500–11000	1998 Mar 1 (3)	20
O4DJ01020	CLEAR-50CCD	51 × 51	...	2130–10270	1997 Nov 16 (1)	120
O4DJ01030	CLEAR-50CCD	51 × 51	G430M	4950–5236	1997 Nov 16 (1)	1754
O4DJ01040	CLEAR-50CCD	51 × 51	...	2130–10270	1997 Nov 16 (1)	36
O4DJ01050	CLEAR-50CCD	51 × 51	...	2130–10270	1997 Nov 16 (1)	3.6
O4DJ55F5Q	F25QTZ-MAMA	25 × 25	...	1460–3270	1998 Oct 12 (5)	800

continuum in this region. In the case of the red G750M spectra we adopted a different approach. Since the lines have high equivalent width and the continuum shape is relatively flat and of low S/N, we modeled the continuum as a simple straight-line fit. No continuum subtraction was attempted for the UV G140L data because of its low S/N.

An important task is to define suitable regions to sum along each slit, enabling measurement of weak lines. Three schemes were chosen: one of small regions for measuring strong emission lines ([O II] λ3727, [Ne III] λ3869, Hβ, [O III] λ5007, Hα, and [N II] λ6584), one of larger regions for measuring weak emission lines ([Ne V] λ3426, Hδ, Hγ, [O III] λ4363, He II λ4686, [O I] λ6300, and [S II] λλ6717, 6731), and one of much larger regions for measuring the low-S/N UV lines (Lyα, N V λ1240, Si IV λ1397, C IV λ1549, and He II λ1640).[6] While summing contiguous pixels to boost S/N, we nevertheless tried to ensure that only one basic velocity or ionization "feature" was included in each region. In the UV, however, where no UV lines are visible across the central dusty 2″, the UV measurements were limited to a few large bins on the eastern and western sides.

Figure 2 shows the continuum-subtracted G430L and G750M data and the unsubtracted G140L data for all four slits.

3.2. *Emission-Line Fluxes*

Emission-line fluxes were measured relative to the [O III] λ5007 flux: the [O III] λ5007 line was shifted (in velocity space) and matched to each emission line. Whereas the shift was constrained by the ratio of the rest wavelengths, the height was varied to optimize the fit. Lines in the G750M data were fitted by the [O III] λ5007 line from the G430M data, whereas lines in the G430L data were fitted by the [O III] λ5007 line from the same data. This method works well for weak lines and blended features but requires all emission lines to have the same shape. Although this would be a poor assumption for large apertures (e.g., from ground-based observations), it is, in fact, a good assumption for small apertures that subsample an extended emission region. When the data allow, most profiles in Mrk 78 are indeed found to be very similar (an important fact discussed further in § 6). There are, nevertheless, a few cases in which minor profile differences are seen, although in almost all these cases the comparison is between two different gratings and a region of rapid profile change along the slit. It seems, therefore, that these effects are due, at least in part, to small aperture shifts between exposures. Errors on the [O III] λ5007 flux were estimated from visual uncertainties in wing and continuum placement and the rms noise in the data, following the method outlined in Whittle (1985a). Errors for other lines were estimated by eye from the match to the [O III] profile.

Due to the much lower S/N for the G140L UV data, we adopted a different approach to measuring the UV lines: Lyα was measured by direct integration between the extremities of the two wings, chosen by eye, over a locally fitted continuum, and this profile was then used to match the other UV lines.

3.3. *Continuum and Reddening Measurements*

Finally, emission-line fluxes and flux ratios were corrected for reddening using the reddening law of Cardelli et al. (1989) and values of A_V that were estimated from the Hα/Hβ ratio assuming a case B unreddened value of 2.87. We prefer the case B value to the value of 3.1 often used for Seyfert NLRs (Gaskell & Ferland 1984), since that value is more appropriate for higher density gas closer to the nucleus. Where measurable, the He II λ1640/λ4686 ratio (unreddened value of ∼7) gave consistent values for the reddening, although with significantly larger error.

To evaluate the error on each corrected line ratio, we used a Monte Carlo bootstrap method. This is preferred over a simple "propagation of error" method, which is poorly suited to our situation: ratios multiplied by nonlinear functions of ratios, with potentially large uncertainties on some measurements. Evaluating each ratio 10^4 times, we randomly sampled each emission line assuming Gaussian measurement errors to generate the error distribution. The final value is taken as the median, whereas the 5 and 95 percentile ranges give equivalent 2 σ errors. To maintain clarity in Figures 3–5, we choose *not* to plot these individual errors but instead plot separately a single median error bar for the plotted sample, together with 10th and 90th percentile ranges indicated by smaller dashes.

3.4. *G430M and* [O III] *λ5007 Kinematic Measurements*

The G430M data provide high-dispersion coverage of Hβ and [O III] λλ4959, 5007 and are therefore well suited to kinematic measurements. Although these data are discussed in more detail in Paper III, we briefly discuss them here, since kinematic measurements are also used in the present paper.

The continuum was taken to be a straight line with the gradient and intensity found in the G430L data, since these have the higher continuum S/N. The choice of a straight line, as opposed to stellar template, is irrelevant given the high [O III] λ5007 equivalent width and low continuum S/N. The wavelength

[6] In what follows, we omit the wavelength when referring to an emission line (except [O III] λ4363 and He II λ1640, which remove ambiguity). In addition, "[S II]" refers to the sum of the λ6717 and λ6731 lines.

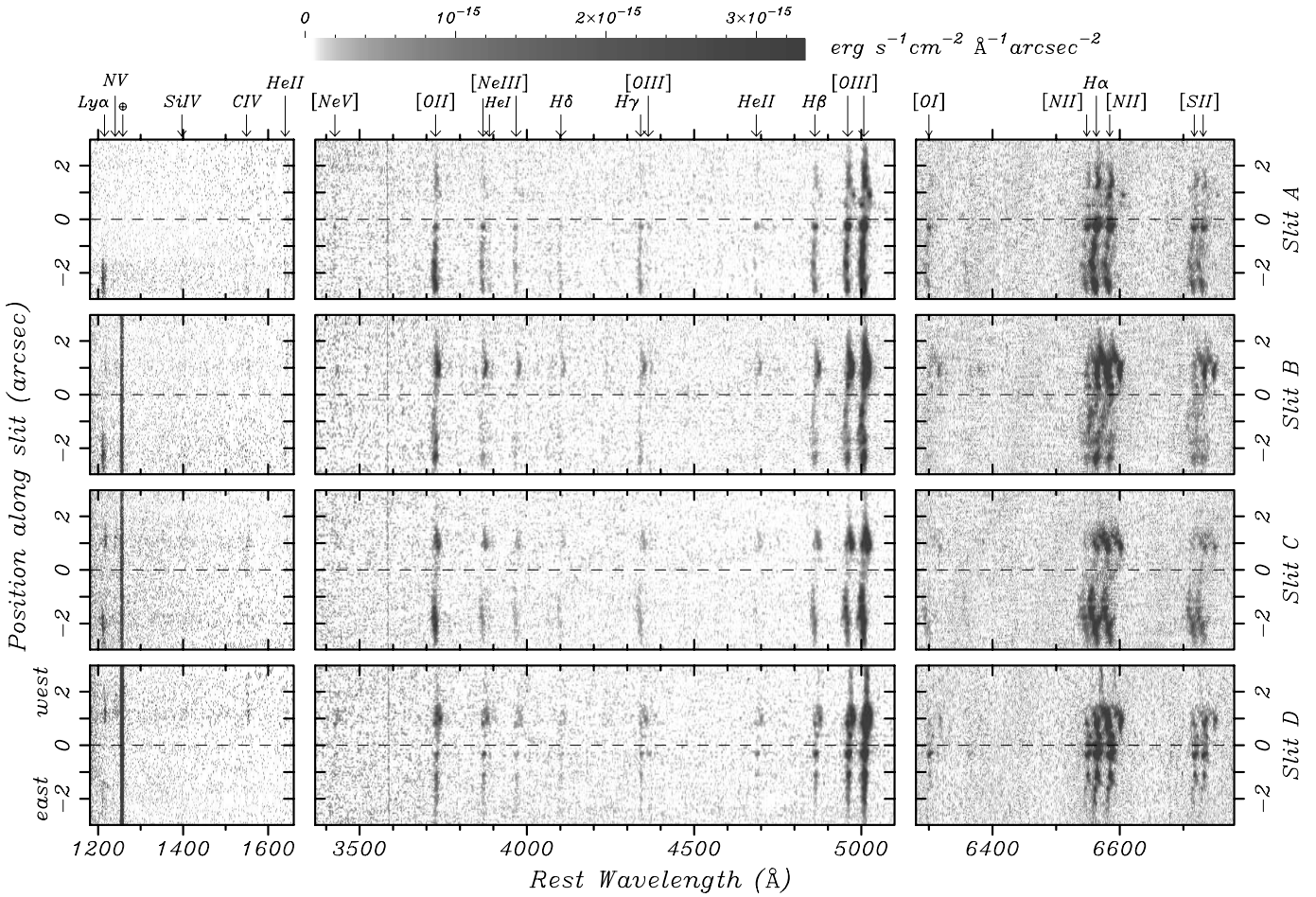

FIG. 2.—Gray-scale presentation of the G140L, G430L, and G750M data from all four slits. The G430L and G750M data have been continuum-subtracted, whereas the G140L data have not. The data have been shifted to rest frame by $cz = 11,052$ km s^{-1}, and major emission lines are indicated. The intensity scale is the same for all images and is shown at the top. In practice, some faint features that are visible in the data are not visible in this figure.

scale was verified by comparing the sum of the three parallel slits (A, B, and C) that match the ground-based data of Whittle et al. (1988). After smoothing and resampling to match the ground-based data (∼1.″7 seeing; 0.″63 square pixels; ∼45 km s^{-1} resolution), the profile distributions were gratifyingly similar and agreed in wavelength to within ∼20 km s^{-1} following a vacuum-to-air shift of −86 km s^{-1} for the STIS data. A number of kinematic parameters were measured from the [O III] λ5007 line profiles, following methods given in Heckman et al. (1981) and Whittle (1985a). For the present discussion, we consider only two: C80 is the line center defined at 80% of the peak height and expressed relative to systemic velocity (11,052 km s^{-1}; Whittle et al. 1988), and FWHM is the line width defined at 50% of the peak height. C80 characterizes the (projected) bulk velocity of the ionized gas, whereas FWHM characterizes its (projected) internal velocity dispersion. Both parameters are easily measured and are relatively insensitive to complexities near the profile base, such as blending or low S/N. In those cases in which blending of multiple components is severe, the profiles were modeled by two or three Gaussians. The instrument resolution is sufficiently high that no resolution corrections were required. Errors in C80 and FWHM were estimated by eye.

3.5. *FOS Data*

The FOS data are described in detail in Paper I, §§ 2.4 and 5, and they are displayed in Figures 6 and 10 of that paper. Briefly, target acquisition failed, and all apertures landed 0.″66 offset in position angle 217° from their intended position (see Figs. 1 and 6 in Paper I). Thus, rather than sampling a set of well defined features, our FOS data sample a rather random set of locations displaced somewhat to the south. Although not ideal, these nevertheless provide useful additions to the STIS data set. In particular, they add spectra away from the main radiation and jet axis and, with their larger aperture size, some provide higher S/Ns, allowing more confident measurements of some of the weaker features.

Since the FOS data were acquired and analyzed some time before the STIS data, our methods were a little different. Our continuum template, for example, was derived from visual fits to the spectrum from aperture 6 using a mix of A1 V, F0 V, G2 III, and K2 III star spectra taken from Jacoby et al. (1984) with relative strengths at 5500 Å of 0.3:1:2:3. With appropriate reddening, this was used for continuum subtraction for all 10 apertures. The method of measuring line fluxes was, however, similar to the STIS data: namely, we shifted and matched the [O III] λ5007 profile to the other lines. As with the STIS data, when the S/N allowed, the forms of all the profiles in each spectrum were found to be very similar.

4. IONIZATION MODELS

In this section we follow the well-known practice of comparing measured emission-line ratios with different ionization models. Our choice of models and line ratios loosely follows

previous work in this area (Baldwin et al. 1981; Ferland & Netzer 1983; Veilleux & Osterbrock 1987; DS95; BWS96). The four classes of model we use to compare with observations are power-law photoionization of optically thick gas, a mixture of optically thin and optically thick photoionized gas, photoionizing shocks, and photoionization of dusty gas in which radiation pressure can be important.

4.1. *U-Photoionization Sequences*

Early models of both narrow- and broad-line region emission in AGNs considered a central source whose power-law (or modified power-law) radiation ionizes surrounding gas clouds that are optically thick to the Lyman continuum. Since the emergent spectrum from these clouds is primarily dependent on the ionization parameter, U (equal to the ionizing photon–to–electron density ratio), a useful sequence of models spans a range of U, with possible parallel sequences using different ionizing spectral shape, gas density, or abundance (e.g., Davidson & Netzer 1979). We evaluated two such sequences, $U_{1.0}$ and $U_{1.4}$, calculated using CLOUDY (Ferland 1996, ver. 90) with power-law spectra of index 1.0 and 1.4 ($F_\nu \propto \nu^{-\alpha}$) and exponential cutoffs below 100 μm and above 50 keV, hydrogen gas densities of 10^2 cm^{-3}, stopping criteria of $\tau_{\rm Lyc} = 10^4$ or $T = 2000$ K (whichever occurs first), and ionization parameters spanning the range $\log U = -4.0$ to $+0.5$. A third sequence was calculated using CLOUDY's modified power law "Table AGN" (which has $\alpha_{\rm ox} = 1.4$ and includes a big blue bump) with results sufficiently similar to the simple $\alpha = 1.4$ power law that we do not discuss it further. Comparison with similar models from BWS96 (using MAPPINGS) shows good agreement for all sequences. Figures 3–6 show only the $U_{1.4}$ sequence, since it is in all cases closer to the data. A limited part of the sequence is plotted (*dotted line*), with a cross, a star, and another cross at $\log U = -3.5$, -2.5, and -1.5, respectively, and a plus sign at other intervals of 0.5 in $\log U$.

4.2. $A_{m/i}$-*Photoionization Sequences*

Although good as a first approximation, the standard single U photoionization models fail to get certain line strengths correct (typically, the temperature diagnostic [O III] λ4363, the He II λ4686/Hβ ratio, and high-ionization lines like [Ne V] λ3426). Perhaps not surprisingly, models that include *two* photoionized components can achieve better overall agreement. One approach is to combine optically thin (i.e., matter-bounded [MB]) gas of high temperature and ionization with optically thick gas (i.e., ionization-bounded [IB]) of lower temperature and ionization. Following initial work by Viegas & Gruenwald (1988), this approach has been more fully developed by BWS96, who suggest that the optically thick gas is itself ionized by the partially absorbed radiation that passes through the optically thin gas. The geometry envisioned involves a nuclear radiation source (power law, $\alpha = 1.3$) and either a physical separation of two cloud types (optically thin/thick clouds further in/out) or single clouds with a dense, optically thick core, surrounded by an evaporating optically thin halo. The ionization parameters and optical depths of the two gas phases are chosen to optimally match observed line ratios: $\log U_{\rm thin} = -1.4$, $\log U_{\rm thick} = -3.3$, $n_{\rm H,thin} = 50$ cm^{-3}, $n_{\rm H,thick} = 2500$ cm^{-3}, $F_{\rm thin} = 0.40$, and $F_{\rm thick} = 0.97$, where F is the fraction of ionizing radiation absorbed by the gas. Each model is defined by the ratio of the solid angles subtended by the thin and thick gas, $A_{m/i}$. Clearly, models of increasing $A_{m/i}$ have increasing excitation and temperature. As it happens, this original $A_{m/i}$ sequence does *not* give a particularly good match for Mrk 78, which has fairly weak high-ionization lines. We therefore used CLOUDY to generate our own sequence, $A'_{m/i}$, optimized to Mrk 78. After first reproducing the original $A_{m/i}$ sequence, we lowered $U_{\rm thin}$ to -1.8 and varied the thin column to recover $F_{\rm thin} = 0.40$, keeping all other parameters constant. Our optimized sequence now matches the weaker [Ne V] and He II lines in Mrk 78, although the match to the [O III] λ4363 line is slightly worse. For clarity, we only show the optimized $A'_{m/i}$ sequence in Figures 3–6. The plot of $A'_{m/i}$ follows the dashed line, with a cross, a star, and another cross at $\log A = -1.0$, 0.0, and +1.0, respectively, and a plus sign at other intervals of 0.5 in $\log A$.

Perhaps the weakness of the $A_{m/i}$ models is their reliance on four narrowly defined parameters, $U_{\rm thin}$, $U_{\rm thick}$, $F_{\rm thin}$, and $F_{\rm thick}$. It is important to establish whether these values might emerge naturally from a more detailed physical analysis of the NLR gas and its environment.

4.3. *Shock Velocity Sequences*

In the study of AGNs, shock-related ionization was first invoked to explain low-ionization, i.e., LINER, spectra (e.g., Fosbury et al. 1978; Heckman 1980). Following models that combined emission from shocks and central source photoionization (e.g., Aldrovandi & Contini 1984, 1985; Viegas-Aldrovandi & Contini 1989a, 1989b), more recent models have been developed that take account of the fact that fast shocks generate sufficient UV and soft X-ray radiation to photoionize both the pre- and postshock gas, producing high-ionization spectra similar to classical AGNs (Sutherland et al. 1993; DS95, DS96). Some of the astrophysical motivation for considering such models includes (1) the desire to find a single mechanism to account for the spectra of Seyfert galaxies, LINERs, and cooling flows, (2) the presence of several correlations between emission-line strengths and gas kinematics, and (3) a number of perceived weaknesses in the standard photoionization scenario. To first order, at least, it seems that these models compete well with the standard central source photoionization models (DS95; Morse et al. 1996).

In Figures 3–6 we take data directly from DS96 for models with shock velocities in the range 200–500 km s^{-1}. The models have preshock gas density of 1 cm^{-3} and solar abundance. Although line emission from the preshock and postshock gas are tabulated separately, here we plot only their sum. Not only is this the most appropriate astrophysical choice, but preshock alone and postshock alone yield poor overall fits to the data. Broadly speaking, the shock velocity sequence yields an excitation sequence in the emitted line ratios. A second parameter, magnetic field, is relevant, since magnetic fields inhibit postshock compression, yielding lower postshock densities. In our figures, we plot only two of the four sequences evaluated by DS96 ($B/\sqrt{n} = 0$ and 2 μG cm$^{3/2}$ for thin and thick solid lines, respectively), since all sequences with nonzero magnetic parameters give similar line ratios, with the exception of ratios that include [O II] λ3727 and [N II] λ6584, which are consistently weaker in fast nonmagnetic shocks. Our figures also include a new sequence of photoionizing shock models that includes significant improvements in the treatment of line and continuum transfer (R. S. Sutherland 2003, private communication; M. G. Allen 2004, private communication). The new sequence has similar input parameters (with magnetic field $B/\sqrt{n} \sim 3$ μG cm$^{3/2}$) but extends up to 1000 km s^{-1} (shown as a separate thick solid line with crosses at 200 and 1000 km s^{-1}).

4.4. $U_{\rm dust}$-*Photoionization Sequences*

Recently, Dopita et al. (2002) and Groves et al. (2004a, 2004b; hereafter GDS04a, GDS04b, respectively), have introduced a variant of the standard optically thick photoionization sequence: specifically, they include a realistic dust content and solve the cloud's ionization structure isobarically. In this scenario, the dust plays an important role, since its high opacity results in a significant radiation pressure gradient. This work uncovers an interesting feedback process: above a certain threshold of *incident* radiation parameter, the internal cloud structure adjusts to yield an effectively constant *internal* radiation parameter, which itself determines many of the observed emission-line strengths. Thus, on line ratio-ratio plots, model sequences tend to stagnate and remain close to certain regions, which, it transpires, are where most Seyfert galaxies lie.

From the range of models given in GDS04a, we choose the one with gas density 10^3 cm^{-3} (defined at the ionization front), power-law index -1.4, and twice solar abundance. Of all the models in GDS04a, this gives the best overall fit to our data set. The choice of density and power-law index allows a simple comparison with our CLOUDY $U_{1.4}$ sequence, whereas the high abundance, as found by GDS04b, is needed to achieve [O III] λ5007/Hβ above 10. In our diagrams, we plot as a dash-dotted line the model line ratios for radiation parameters $\log U_{\rm dust} = -3.0$ to 0.0, with a cross, a star, and another cross at -3.0, -2.0, and 0.0. Note that because of the "saturation" effect, the trajectories often turn around and can even reverse direction.

5. LINE RATIO DIAGRAMS

Figures 3–6 show important ratio-ratio plots for the STIS and FOS data with the three classes of model sequences superposed. The FOS and STIS data on Mrk 78 are well suited to this kind of analysis, principally because it is *spatially resolved*. Each aperture samples a narrow range of gas properties, and the gas density is low enough to avoid ambiguities arising from collisional suppression of forbidden lines. This contrasts with typical nuclear spectroscopy, which samples a wide range in conditions, including high gas densities (as inferred from line profile differences; e.g., Filippenko & Halpern 1984; Whittle 1985b). Not only do our apertures avoid the nucleus, they also avoid the extended narrow-line region (ENLR), which, for Seyfert galaxies, is located *beyond* the region of direct influence of the inner radio source (e.g., Unger et al. 1987) and is therefore of secondary interest in this study. Thus, we sample genuine NLR gas on intermediate scales associated with the radio source using relatively clean diagnostics. We hope, therefore, that our results will apply to Seyfert NLRs in general.

Only reddening-corrected values are shown, together with the median 2 σ error bar and its 10th and 90th percentile range for each plotted subsample. We divide the line ratios into groups that help clarify the overall analysis.

5.1. *Traditional Excitation Diagnostics*

Figures 3*a* and 3*b* show ratios that highlight overall ionization level: [O III]/Hβ versus [O III]/[O II] and [O III]/Hβ versus [Ne III]/[O II]. All models follow approximately the same diagonal trend of increasing excitation from low to high values of U, $A_{m/i}$, and shock velocity. The data span a decade range in the primary excitation ratios and nicely follow the curves of the photoionization sequences, both for $A_{m/i}$ and U. There appears to be a significant preference for the $\alpha = 1.4$ sequence over the $\alpha = 1.0$ sequence (not shown) and a marginal preference for the revised $A'_{m/i}$ sequence over the original (BWS96) $A_{m/i}$ sequence (also not shown). The old shock models fit reasonably well, although the new shock models do not reach high enough excitation and are clearly ruled out. Quantifying the model fits, the data span $\log U_{1.4} \sim -3.0$ to -2.0 and $\log A'_{m/i} \sim -0.5$ to +1.0, whereas shock velocities are $\sim$300–500 km s^{-1} for the old models. For these old shock models, the effect of the magnetic field is particularly notable, with collisional suppression of [O II] increasing for high velocities in the zero B shock.

The case for the $U_{\rm dust}$ sequence is not straightforward. Both [O III]/[O II] and [Ne III]/[O II] present problems. For the former, the fit is good for the low- and intermediate-excitation regions, but the model cannot provide log [O III]/[O II] above 0.8—sufficient for most single-aperture Seyfert data, but not for the high-ionization inner regions of Mrk 78. In addition, [Ne III] λ3868 is consistently too strong in the $U_{\rm dust}$ models by $\sim$0.5 dex, suggesting [O II] and [Ne III] have comparable strength. We are unsure how to interpret this latter problem with the dusty models, in part because GDS04b only discuss [Ne III] in combination with [Ne V].

5.2. *The* [O I] λ*6300 Line*

Figures 3*c* and 3*d* show two common diagrams that include the [O I] line: [O III]/Hβ versus [O III]/[O I] and [O III]/Hβ versus [O I]/Hα. In both cases the data follow approximately the $A'_{m/i}$ and $U_{1.4}$ sequences, spanning $\log U \sim -3.2$ to -2.2 and $\log A \sim -0.5$ to +0.7, essentially consistent with the previous two diagrams. As before, the $U_{1.4}$ sequence provides a significantly better fit than the $U_{1.0}$ sequence. As is now well known, the shock models provide a very poor match to the data: not only are the observed trends orthogonal to the shock models, but they overpredict the [O I] λ6300 line strength by about a factor of 10. We also find that the $U_{\rm dust}$ sequence has problems, curving away from the data in both diagrams. As discussed by GDS04b, steeper power laws and lower abundance bring the models closer to the data.

It is unclear how much significance to give to these mismatches in [O I] strength, which are also found in other objects. It is generally acknowledged that treatment of the [O I] line can be difficult in all types of models, photoionization as well as shock. In addition to a number of difficulties specific to the shock models (see DS96), in photoionization models the [O I] line is sensitive to details of the high-energy spectral shape and the depth of the cloud, since it is formed in a partially ionized ("transition") region kept warm by X-ray heating. It may be wise, therefore, not to place too much emphasis on this line when comparing models and data. Having said that, however, when data from a single object define a clear trend that falls along a model sequence (as it does in Fig. 3*c*, for example) the simple inference that the model might be relevant seems reasonable.

5.3. *Separating the Sequences*

Figures 4*a* and 4*b* show diagrams in which the shock sequences lie at a large angle to the $U_{1.4}$ and $A'_{m/i}$ sequences: Hα/[N II] versus [O III]/[N II] and [O III]/Hβ versus [S II]/Hα. The important result is that the data form clear trends that follow the directions of the $U_{1.4}$ and $A'_{m/i}$ sequences and show essentially no connection to the shock sequences. Not only do the data trends lie almost orthogonal to the shock sequences, but they also inhabit different parts of the diagram. In Figure 4*a* the new shock sequence fails to reach high enough excitation,

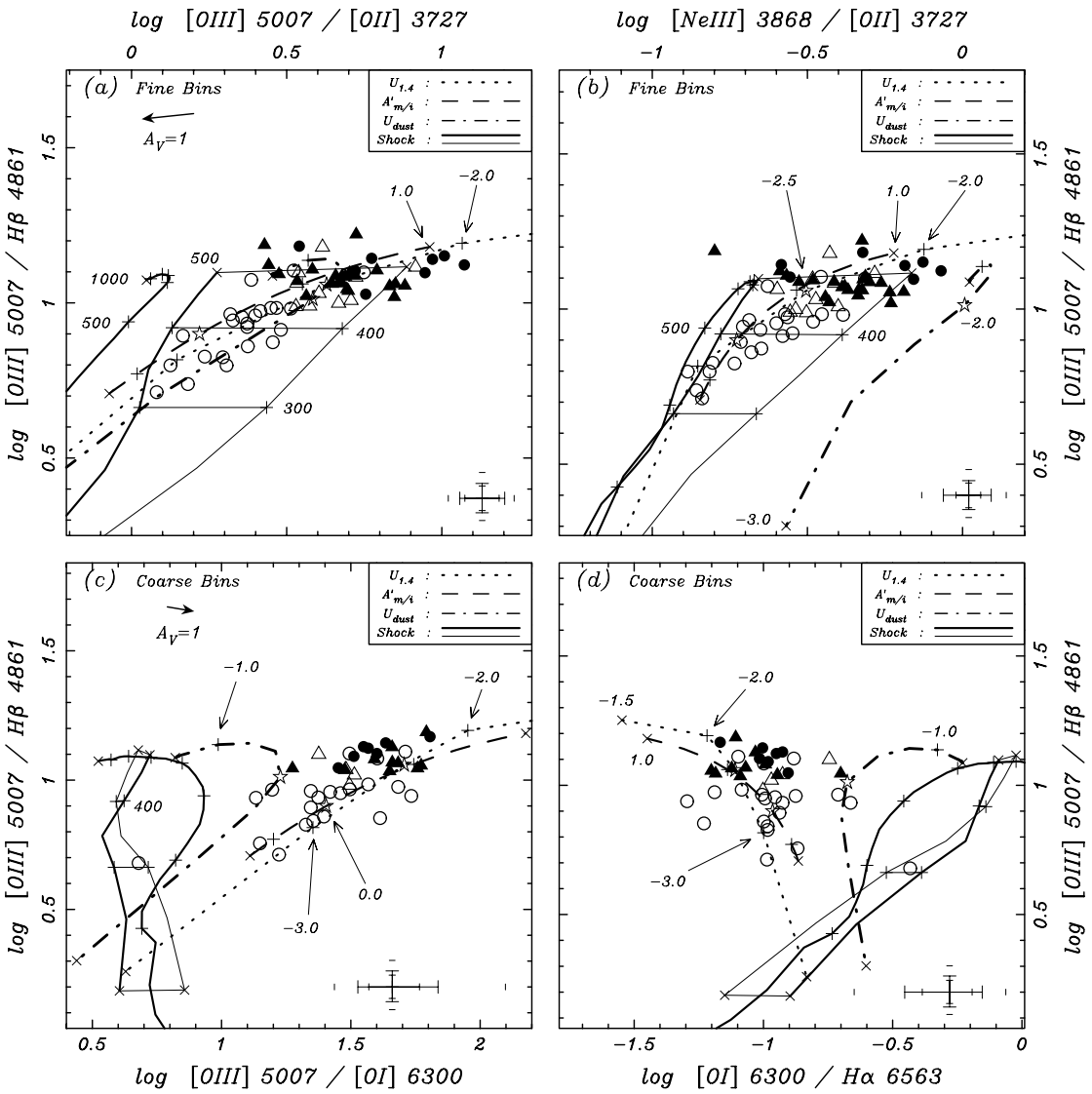

FIG. 3.—Emission-line ratio-ratio plots of traditional excitation and [O I] diagnostics. Triangles and circles are for east and west locations, whereas filled and open symbols are for inner and outer regions (e.g., inner and outer eastern fan, inner and outer western lobe). Bin choice is indicated (fine bins for strong lines and coarse bins for weak lines; see § 3.1). All data have been corrected for reddening, and when significant, we show a reddening vector corresponding to $A_V = 1$ mag. The median 2 σ error bar for the plotted points is shown, with smaller ticks indicating the 10% and 90% range. Four model sequences are shown (see text for details): optically thick photoionization by an AGN power law ($U_{1.4}$; *dotted line*); an optically thick and thin mix photoionized by an AGN power law ($A'_{m/i}$; *dashed line*); AGN power-law photoionized dusty gas with radiation pressure ($U_{\rm dust}$; *dot-dashed line*); and photoionizing shocks from DS95 and M. G. Allen (2004, private communication) (*solid lines*; thin [nonmagnetic] connected to thick [magnetic], with the newer [magnetic] models shown as the stand-alone thick solid line). Symbols plotted on each sequence help identify the parameter values, with a cross at each end and a star for the central value ($\log U_{1.4} = -1.5$, -2.5, and -3.5; $\log A = -1.0$, 0.0, and +1.0; and $\log U_{\rm dust} = -3.0$, -2.0, and 0.0, respectively), with plus signs every 0.5 dex (1.0 dex for the $U_{\rm dust}$ models). The shock sequences span 200–500 km s^{-1} (original) and 200–1000 km s^{-1} (new), with plus signs every 100 km s^{-1}. Some specific values are labeled.

even at 1000 km s^{-1}, whereas in Figure 4*b* the shock models only intersect the lowest excitation data. It is these diagrams that provide the most serious challenge for the shock models.

Can magnetic fields help the shock models? Not really. Although in Figure 4*a* it seems that a series of increasing magnetic fields in 400–500 km s^{-1} shocks might span the data, this is not really the case, since all nonzero B shock sequences fall close to the $B/\sqrt{n} = 2$ example plotted. Furthermore, Figure 4*b* shows almost no dependence of [S II]/Hα on magnetic parameters. (This dependence sets in at higher preshock densities, above 100 cm^{-3}, although in that case [S II]/Hα values drop below all our data points.)

Turning to the U and $A_{m/i}$ sequences: are these diagrams consistent with the previous ones? For Figure 4*b* the answer is yes: the data span similar ranges in $\log U_{1.4}$ and $\log A$, follow the $U_{1.4}$ sequence more closely than $U_{1.0}$, and show a marginal preference for the optimized $A'_{m/i}$ sequence. Interestingly, Figure 4*a* is *not* consistent with the previous diagrams: the inferred parameter ranges are lower than the other diagrams by $\sim$0.4 dex in both $\log U_{1.4}$ and $\log A$, and the data seem to lie closer to the $U_{1.0}$ and old $A_{m/i}$ sequences (not shown). As we discuss in the next section, all these inconsistencies can be understood once we correct for an enhanced nuclear nitrogen abundance.

The $U_{\rm dust}$ sequence shows intermediate success. In Figure 4*a* the sequence passes through the data but fails to reach the highest excitation points. In Figure 4*b* the sequence overpredicts [S II] by $\sim$0.2–0.5 dex (yielding [S II] comparable to Hα), although, as with [O I], a steeper power-law index and/or lower

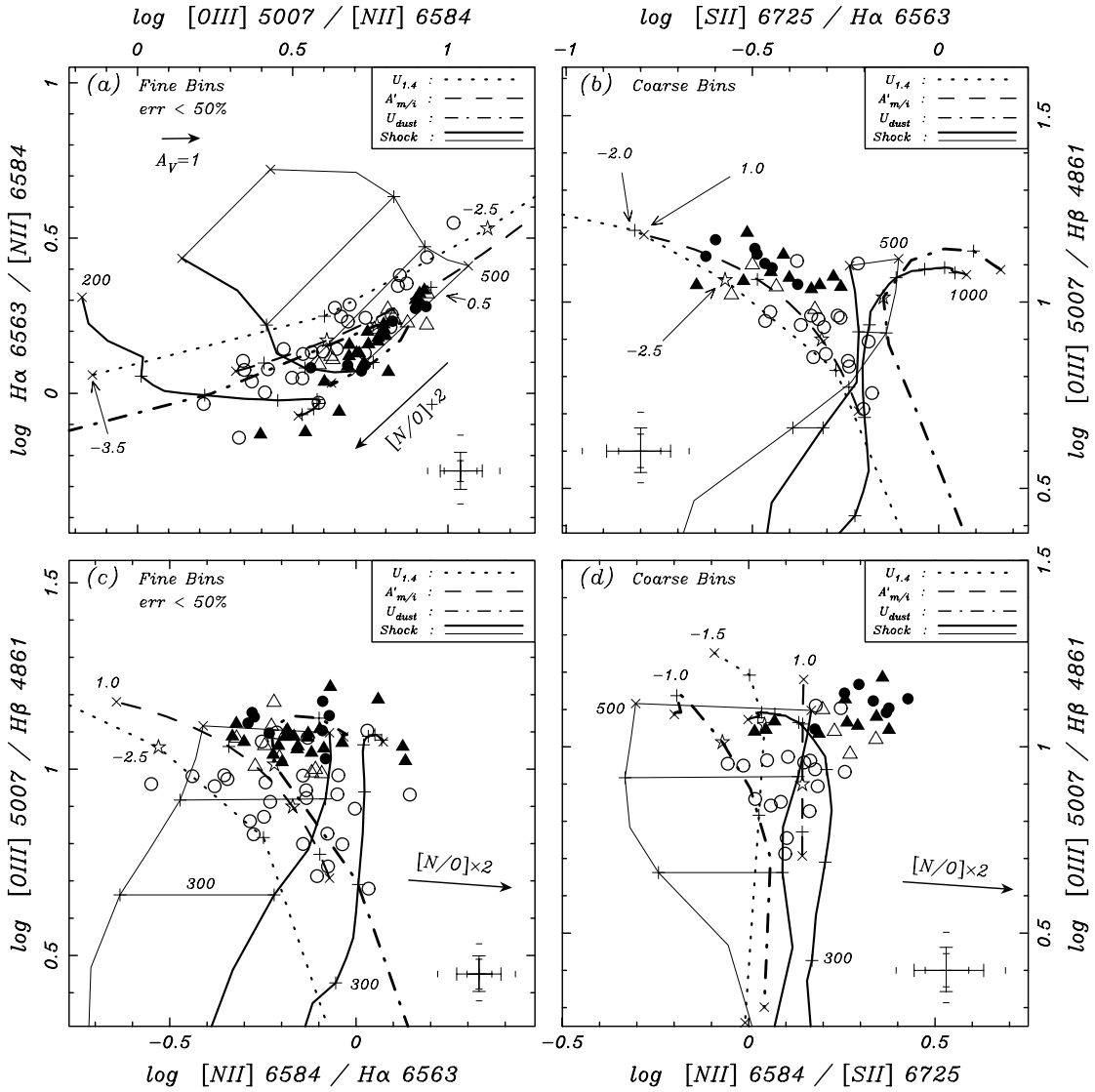

FIG. 4.—Emission-line ratio-ratio plots that separate photoionization and shocks (panels *a*, *b*, and *c*) and that explore nitrogen abundance (panels *a*, *c*, and *d*). See caption to Fig. 3 for details.

abundance helps reduce the gap. Even so, at higher excitation, the *trend* of the data is *opposite* to the trend of the $U_{\rm dust}$ sequence. Ironically, it is precisely the stagnation characteristic of the $U_{\rm dust}$ models that leads to this difficulty, whereas the standard photoionization models nicely follow the data trend to lower [S II]/Hα at higher excitation.

5.4. *The* [N II] *λ6584 Line and Nitrogen Abundance*

Figure 4*c* shows [O III]/Hβ versus [N II]/Hα. The data span a significant range but show no trend. Although they scatter around the photoionization models, they are offset somewhat compared with the previous plots, lying closer to the $U_{1.0}$ sequence, with $\log U_{1.4} = -2.6$ as a maximum. If we interpret this offset in terms of an enhanced [N II] strength, we require an enhancement ranging from $\sim$0.4 dex (at highest [O III]/Hβ) to $\sim$0 dex (at lowest [O III]/Hβ). As we see in § 7.2, the trend in [O III]/Hβ corresponds to a *radial* decrease in excitation, and hence these offsets are largest closest to the nucleus, as is also clear from the separation of the various plot symbols. The enhancement of nuclear [N II]/Hα ratios over standard models is frequently observed in Seyfert galaxies and LINERs and is usually explained as an enhanced N/O abundance ratio in the nuclear regions of luminous galaxies (e.g., Pagel & Edmunds 1981; Storchi-Bergmann et al. 1996a; Kraemer et al. 1998).

This effect is also seen clearly in Figure 4*d*, which plots [O III]/Hβ versus [N II]/[S II]. All three types of photoionization model have approximately constant [N II]/[S II] ratio, and yet the data show a clear diagonal trend. Once again, if the data are offset by $\sim$0.3 dex for the most nuclear (highest excitation) apertures, then the data become parallel to the models and lie between the $U_{1.4}$ and optimized $A'_{m/i}$ sequences. To illustrate the effect of enhanced nitrogen abundance, we ran a second set of $\alpha = 1.4$ CLOUDY models with doubled N/O. The vectors plotted on Figures 4*c* and 4*d* show the offset and suggest a nitrogen overabundance of about 2 times in the nucleus of Mrk 78. We explore radial gradients more generally in § 7.2, where we indeed find a decrease in the [N II]/[S II] ratio with increasing distance from the nucleus (see Fig. 9*d*). Since this ratio is insensitive to both excitation and reddening, it provides a good diagnostic of the nitrogen abundance, which is seen to rise by roughly a factor of 2 toward the nucleus.

The behavior of the dusty photoionization model is interesting but complex. First, although our chosen model has 2 times solar abundance, the nitrogen abundance is more like 3 times solar, since GDS04a allow for its secondary nature. Thus, in Figure 4*c*, the $U_{\rm dust}$ sequence has already benefited from the enhanced nitrogen "fix" described above, and indeed the 1 times solar model is a very poor fit. Despite the enhanced nitrogen, however, the [N II]/[S II] sequence in Figure 4*d* is *still* not particularly good, veering away from the data at high excitation. This is almost certainly because [S II] is overpredicted in the dusty models, as indicated in Figure 4*b*.

Turning to the shock models, we find a good match to the data for magnetized shocks in both Figures 4*c* and 4*d*, although as usual they do not achieve high enough excitation even at high shock velocities. Perhaps of more interest is the large separation of nonmagnetic and magnetic shocks in Figure 4*d*, due to the collisional suppression of [N II] λ6584 in the nonmagnetic shocks. If shocks are important, then our data clearly favor magnetic shocks.

5.5. *Model Discriminators:* [O III] λ4363, He II, *and* [Ne V]

We now turn to three emission lines that have consistently caused problems for the standard photoionization models and which, to some extent, have motivated work to find alternative solutions.

Figure 5*a* shows [O III] λ5007/Hβ plotted against the classic temperature diagnostic, $R_{[\rm O\ III]} \equiv$ [O III] λ4363/λ5007. Our data are significantly offset from the $U_{1.4}$ sequences by $\sim$0.4 dex, somewhat offset from the shock and $U_{\rm dust}$ sequences by $\sim$0.2 dex, and scatter nicely between the original $A_{m/i}$ (not shown) and optimized $A'_{m/i}$ sequences. Our data fall in a region that is occupied by both nuclear and ENLR data from Seyfert and radio galaxies in general, and its offset from the $U_{1.4}$ sequence constitutes the well-known [O III] temperature problem (e.g., Tadhunter et al. 1989). For single-aperture nuclear data, the high values of $R_{[\rm O\ III]}$ can be explained by the contribution from high-density gas in which the [O III] λ5007 line is collisionally suppressed (e.g., Filippenko & Halpern 1984). However, the ENLR emission comes from low-density gas, so the high $R_{[\rm O\ III]}$ values unambiguously indicate higher O^{2+} temperatures. Additional heating from radio-source cosmic rays can increase $R_{[\rm O\ III]}$, but this also increases the strengths of the low-ionization lines to unacceptable levels (Ferland & Mushotsky 1984). Subsolar metallicity reduces cooling and so increases $R_{[\rm O\ III]}$ (e.g., Tadhunter et al. 1989). However, the magnitude of the required correction would cause problems with other line ratios.

The apparent solution to the [O III] temperature problem is quite different for the three new classes of model. For shocks, it is the contribution from hot gas in the postshock flow. For the $U_{\rm dust}$ models it is mainly photoelectric heating from dust, and for the $A_{m/i}$ sequence it is the high temperature of the optically thin component. Although the three model trajectories all skirt the data area, plausible modifications can help improve their performance. For example, dropping the abundance to 1 times solar brings the $U_{\rm dust}$ sequence through the data, whereas the $A_{m/i}$ and $A'_{m/i}$ sequences taken together span all the data. Our [O III] λ4363 data, then, seem to exclude the standard optically thick $U_{1.4}$ sequence, but beyond that, one cannot easily distinguish between the other three models.

The He II λ4686 line has received considerable attention recently, since it behaves differently in different models. In particular, the He II/Hβ ratio is roughly independent of U in the standard photoionization models (although it is dependent on spectral index). Consequently, the large spread in observed nuclear values (e.g., Stasinska 1984) and the existence of both higher (BWS96) and lower (e.g., Clark et al. 1998) ENLR values calls standard photoionization into question and motivates the search for alternatives. As it happens, our data are reasonably consistent with the $U_{1.4}$ sequence (although it does scatter to either side), and in most diagrams the data lie close to the intersection of the $U_{1.4}$, $A'_{m/i}$, and shock models (e.g., Fig. 5*b* shows He II/Hβ vs. [O III]/Hβ).[7] There is, however, a weak trend in the data that lends support to the $A_{m/i}$ models over the $U_{1.4}$ models. This preference, however, is not so obvious in related diagrams with other excitation ratios (e.g., He II/Hβ vs. [O III]/[O II] or [Ne III]/[O II]; not shown) in which the data can lie between the $A'_{m/i}$ and $U_{1.4}$ sequences with only a marginal trend. In addition, the He II/Hβ ratios in Mrk 78 are *lower* than the average for Seyfert galaxies by $\sim$0.3 dex and so are *not* well fitted by the original $A_{m/i}$ sequence of BWS96. Our optimized $A'_{m/i}$ sequence fits much better, as expected, since this was one of our targeted ratios to match. The $U_{\rm dust}$ sequences give significantly worse fits to the Mrk 78 data, unable to provide simultaneously high [O III]/Hβ and low He II/Hβ. Exploring other power-law indices or abundances only worsens the fit.

The third potential problem for the standard U models is their inability to reproduce strong high-excitation lines (e.g., [Ne V] λ3426, C IV λ1459, C III] λ1909, [Fe VII] λ6087). Figures 5*c* and 5*d* show excitation diagrams that incorporate the [Ne V] λ3426 line: [O III]/Hβ versus [Ne V]/Hβ and [Ne V]/[Ne III] versus [Ne III]/[O II]. These diagrams are particularly useful because the ratio trajectories are quite sensitive to details of the various models. Furthermore, the second diagram is relatively insensitive to reddening, abundance, and calibration errors. Consider first the standard $U_{1.4}$ and original $A_{m/i}$ models (BWS96, not shown)—our data fall between the two sequences, inconsistent with both, but in opposite senses: the measured [Ne V] ratios would have to be 15 times lower and 5 times higher, respectively, to bring them into alignment with the appropriate $U_{1.4}$ and $A_{m/i}$ parameter ranges. The discrepancy with the U sequence is well known, but the discrepancy with the $A_{m/i}$ sequence is specific to Mrk 78, since BWS96 designed their $A_{m/i}$ sequence to match typical [Ne V] line strengths (along with He II and [O III] λ4363 line strengths). Mrk 78 has unusually weak [Ne V], with [Ne V]/Hβ and [Ne V]/[Ne III] ratios at the lower end of the range found for Seyfert 2 galaxies, $\sim$0.5 dex below the median. Of course, boosting the [Ne V] line strengths only exacerbates the failure of the U sequences. The [Ne V] discrepancy with the standard $A_{m/i}$ sequence was the principal motivation for us to find a revised sequence, $A'_{m/i}$: one with a lower ionization parameter for the optically thin component. Our optimized $A'_{m/i}$ sequence is seen to nicely match our data, including its trend and even its curvature, yielding consistent parameters ($\log A$ from -0.2 to $+1.0$).

The $U_{\rm dust}$ sequence reproduces the [Ne V]/Hβ strengths quite well and certainly better than the normal $U_{1.4}$ sequence. As GDS04a discuss, dust preferentially removes low-energy photons, hardening the internal radiation field and boosting the relative strength of [Ne V]. Figure 5*d* is unfortunately compromised by including [Ne III], which we know to be badly overpredicted (see § 5.1).

[7] We note that, as recommended in the documentation for CLOUDY (Hazy; Ferland 1996), we took the case B He II λ4686 values and not the output from the 10-level atom, "TOTL 4686," which is less reliable at these low densities.

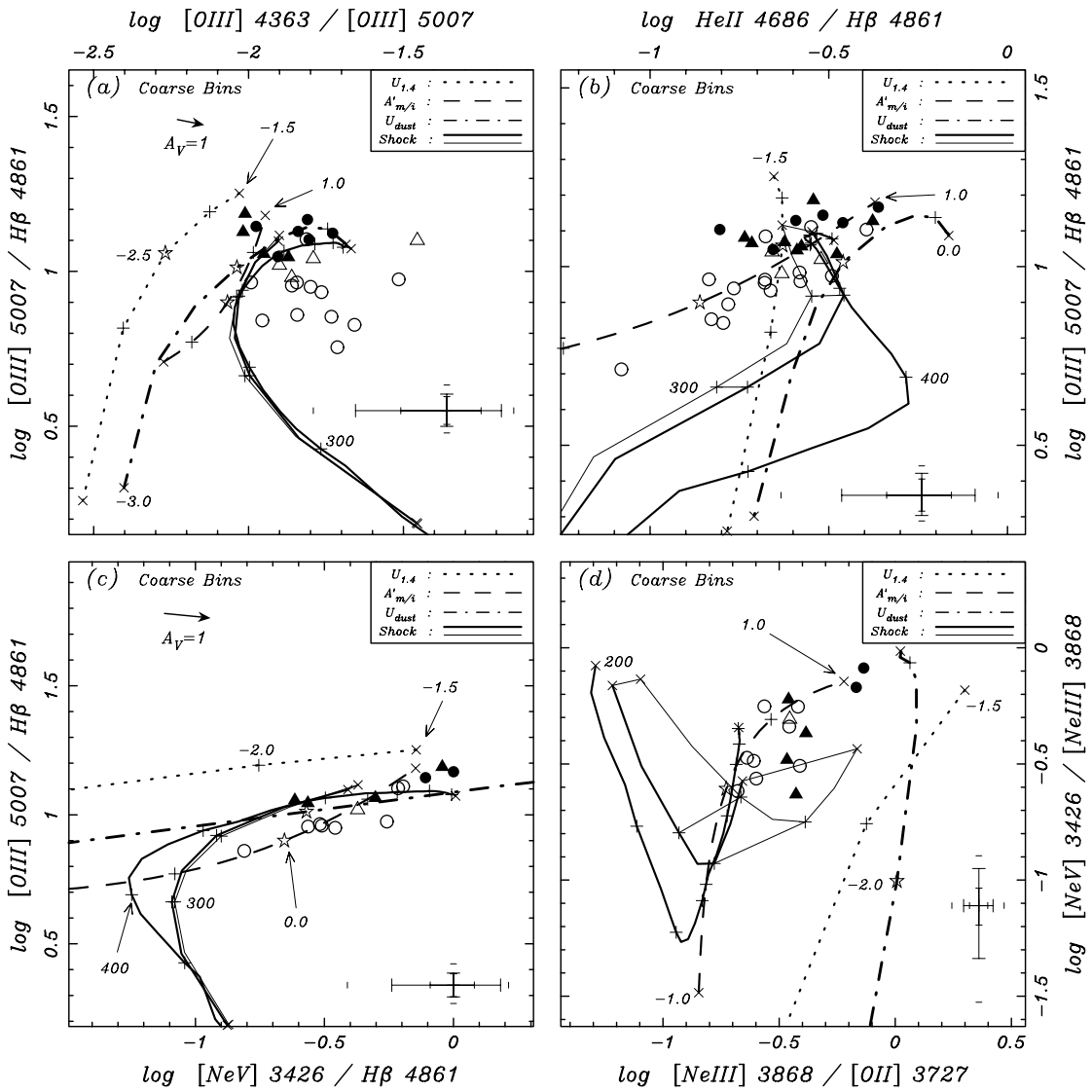

FIG. 5.—Emission-line ratio-ratio plots that help to separate $U_{1.4}$ and $A'_{m/i}$ sequences. See caption to Fig. 3 for details.

Turning to the shock models, although [Ne v] was not explicitly discussed by DS96, it is an interesting line for shock models, since it is relatively strong both in low-velocity shocks (where it comes from the postshock region) and high-velocity shocks (where it comes from the preshock region). Unlike photoionization models, therefore, shock models predict a relatively narrow range of [Ne v] ratios. As it happens, the shock models provide a reasonably good match to our data: they overlap and even show a similar trend, although the models fail to yield the highest ratios. This failure would, of course, be greatly exacerbated for objects with more normal [Ne v] line strengths. Given that, and the poor fits in other diagrams, one should probably consider the match in this case to be fortuitous.

5.6. *UV Lines:* Lyα, N v, C iv, *and* He ii

It has long been recognized that to first order the optical emission lines from fast shocks and power-law photoionization are very similar, in part because much of the emission associated with shocks comes from upstream gas photoionized by a fairly hard spectrum emerging from the hot postshock gas. However, as stressed by Allen et al. (1998), collisionally excited UV resonance lines are likely to be significantly stronger in shocked gas than photoionized gas because of the higher temperature of the post shock gas. Our own UV data help in this regard, although with some limitations: the data are of very low S/N; the G140L grating includes only Lyα, N v, C iv, and He ii; and nuclear dust completely obscures the inner regions, allowing access only to the eastern fan and outer western lobe. Our data, therefore, require rather coarse binning and line ratios not too separated in wavelength to avoid excessive reddening uncertainties.

Figures 6*a*–6*d* show a subset of the various possible UV line ratio diagrams. We confirm the oft-noted difficulty of predicting Lyα: Figures 6*a* and 6*b* show significant offsets from all models for ratios including Hβ, He ii λ1640, and C iv. Although it is possible that we have underestimated the reddening, we feel this is unlikely: the measured data come from large radii at which optical estimates of A_V are both low and quite accurate (the errors are much less than the *additional* 1–2 mag required to fit the models). Furthermore, the N v λ1240 line at a similar wavelength is already too *strong* compared with most models, and further reddening corrections would only exacerbate this difference. Rather, we suspect that the Lyα line does not have its case B value ($\sim$26 relative to Hβ for $n_e = 10^3$ cm^{-3}, $T = 10^4$ K;

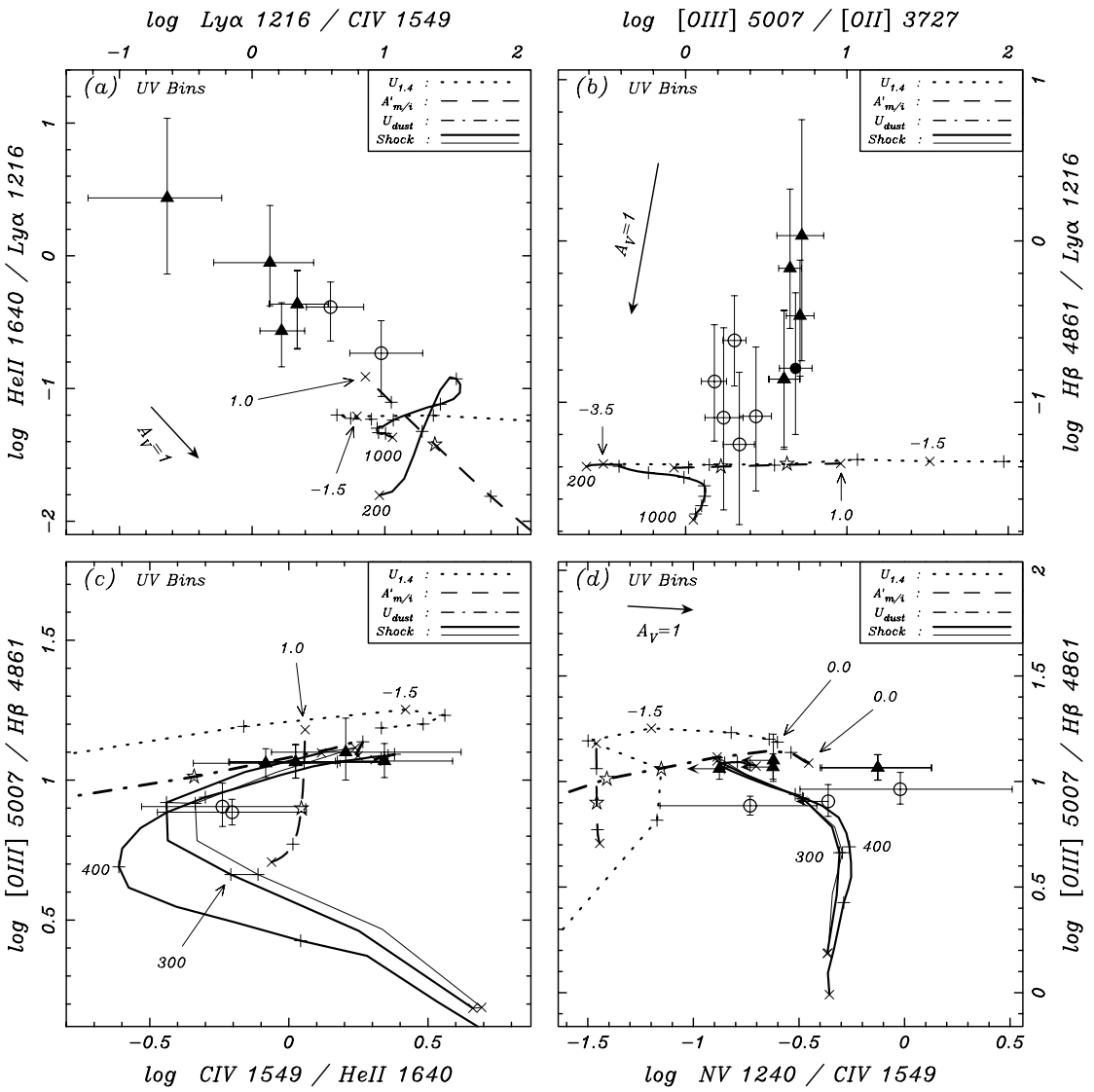

FIG. 6.—Emission-line ratio-ratio plots that include the stronger UV lines. See caption to Fig. 3 for details.

Dopita & Sutherland 2003), probably because of destruction over the long path lengths associated with resonant scattering. This observational uncertainty in the use of Lyα is matched by related uncertainties in the theoretical model predictions, whose authors frequently express concern about (and may therefore not even quote) their calculated Lyα strengths (e.g., Villar-Martín et al. 1996). For this reason, we choose not to pursue the use of Lyα further, except to note that there is some evidence that the Lyα destruction may be systematically higher in the eastern fan (Fig. 6*b*, *triangles*; $\langle \mathrm{Ly}\alpha/\mathrm{H}\beta \rangle \sim 2$) compared with the western lobe (Fig. 6*b*, *circles*; $\langle \mathrm{Ly}\alpha/\mathrm{H}\beta \rangle \sim 10$).

Figure 6*c* shows [O III]/Hβ versus C IV/He II λ1640, together with the various models. Although the data lie close to all models, the proximity to the $U_{1.4}$ sequence is misleading, since the implied values of log U are significantly higher (-1.2) than the optimum values of log U found for the lower ionization optical lines (-3 to -2). The match to the $A'_{m/i}$, shock, and U_{dust} sequences is more genuine and arises, of course, because they each include higher ionization components: the optically thin component of the $A'_{m/i}$ sequence, the hot postshock gas in the shock sequence, and the hardened internal radiation field of the dusty clouds. Although the greater strength of the C IV and other UV resonance lines had originally been suggested as a clear signature of shocks (DS96), as Allen et al. (1998) discuss, this conclusion is no longer unambiguous if one considers either optically thin gas or optically thick gas of very high ionization parameter. (We have extended the $U_{1.4}$ sequence to log $U = 0.0$ in Fig. 6 to show this.)

Finally, Figure 6*d* shows [O III]/Hβ versus N V/C IV. It is perhaps surprising that this diagram has not been discussed more often, since it provides a clear test for shocks that are comparatively efficient producers of N V. Although our standard values of $U_{1.4}$, U_{dust}, and $A'_{m/i}$, matching other line ratios, suggest N V/C IV ~ 0.04, the shock sequences have values 10 times higher for slow shocks, dropping to 3 times higher for fast shocks (increasing again for even faster shocks, as photoionization of the downstream gas increases). With the exception of very high values of log U ($\gtrsim -1.0$ for $U_{1.4}$ and $\gtrsim -1.5$ for U_{dust}), strong N V (and associated high values of N V/C IV) is a strong signature for shocks. Conversely, and more usefully, *a low value of* N V/C IV *unambiguously excludes shocks as a possible dominant contribution*. The only caveat is that the N V strength may also, of course, be subject to increased nuclear nitrogen abundance.

Unfortunately, our data on N v do not give a clear result: four apertures give upper limits (one of which may exclude shocks), whereas three suggest strong N v, two even approaching the strength of C IV. Such ratios would indicate a contribution of shocks in these regions. Three aspects introduce a note of caution, however. First, although we feel the N v line is present, it is undeniably close to the detection limit and falls close to a strong geocoronal line. Second, the detections show no coherent spatial pattern, with both limits and detections on the eastern fan and western lobe. Third, the apparent nitrogen abundance enhancement may artificially boost the N v/C IV ratio. At this stage, therefore, our N v results remain inconclusive: there seems to be weak evidence, which needs confirmation, for a shock contribution in some regions. Of course, the overall evidence supporting photoionization (with optically thin contributions) suggests that, if confirmed, the shock contribution is, in any case, likely to be minor.

While discussing the N v λ1240 line, it is perhaps worth noting that among the rather few UV data sets available for Seyfert NLRs, the N v line is usually below the (admittedly often poor) detection limit, and when it is detected it is usually weak compared with C IV (one exception is NGC 1068, which we discuss below). Although this requires a formal analysis, it does suggest that the N v/C IV ratio is usually low, indicating a limited contribution, if any, from shocks in most objects.

5.7. *Summary of Line Ratio Analysis*

Our line ratio analysis has proved quite successful at discriminating between the various models considered. Briefly, (1) there is a clear overall preference for our optimized $A'_{m/i}$ sequence, (2) a single range of $A'_{m/i}$ parameters accounts for essentially all measured line ratios, and (3) a number of line ratios explicitly exclude the $U_{1.4}$, $U_{\rm dust}$, and shock sequences. The main reason our analysis has been more definitive than many other studies (which often cannot separate the shock and $A_{m/i}$ sequences) is that our data spans a sufficient range of conditions within a single object to provide *trends* on the ratio-ratio plots. Such trends can identify one model over another, even in regions in which the models tend to overlap.

Since this section has been somewhat detailed, we briefly summarize the main points. Standard excitation diagrams (Figs. 3*a* and 3*b*) show a significant range in excitation within the NLR of Mrk 78 (higher nearer the nucleus; see § 7.2 below). To first order, all models follow these excitation trends, although the $U_{\rm dust}$ models significantly overpredict [Ne III]. Introducing the [O I] λ6300 line (Figs. 3*c* and 3*d*) confirms the trends along the $U_{1.4}$ and $A'_{m/i}$ sequences but introduces major problems for the shock and $U_{\rm dust}$ models. Given the theoretical uncertainties for this line, we do not yet regard the mismatch in [O I] as fatal for the shock or $U_{\rm dust}$ models. Together these diagrams indicate that log A spans -0.5 to $+1.0$ and log $U_{1.4}$ spans -3.0 to -2.0, with a clear preference for the canonical $\alpha = 1.4$ power law over the flatter $\alpha = 1.0$.

We introduce two diagrams (Figs. 4*a* and 4*b*) in which the shock sequences lie along a different direction to the $U_{1.4}$ and $A_{m/i}$ sequences. On these plots, the data clearly lie along the $U_{1.4}$ and $A'_{m/i}$ sequences but are significantly at odds with the shock sequences, both in overall position and direction of the trends. These are the fatal diagrams for the shock sequences. Figure 4*b* also poses a serious problem for the $U_{\rm dust}$ models, which not only overpredict the [S II] strength but, more importantly, their defining characteristic sends the sequence along the *wrong* direction with increasing excitation, a feature the standard photoionization models get correct.

We consider two further diagrams that include the [N II] line (Figs. 4*c* and 4*d*) only to find significant mismatch, both with the previously identified ranges in $U_{1.4}$ and $A'_{m/i}$, as well as data trend directions that differ from all models. These differences can be understood in terms of a gradient in the nitrogen abundance, increasing toward the nucleus (and therefore increasing with excitation). Allowing for this abundance variation recovers the data's consistency with the $U_{1.4}$ and $A'_{m/i}$ models. The $U_{\rm dust}$ models also confirm the need for high nitrogen abundance.

Introducing the classic model discriminators [O III] λ4363, He II, and [Ne v] (Figs. 5*a*–5*d*) confirms the well-known inadequacy of the classic U sequence: for normal values of $U_{1.4}$, the predicted temperatures are too low, and the high-excitation lines are too weak. The latter problem also uncovers the inadequacy of the original $A_{m/i}$ sequence created by BWS96, which was optimized to an average Seyfert 2 galaxy with somewhat stronger [Ne v] and He II than Mrk 78. Our revised $A'_{m/i}$ sequence (with reduced ionization parameter for the optically thin component) now fits the data extremely well: not only are the values of log $A'_{m/i}$ consistent with all the previous ratios, but in the He II and [Ne v] diagrams the data form clear trends that lie exactly along the $A'_{m/i}$ sequence. Although the $U_{\rm dust}$ model adequately matches the [O III] λ4363 and [Ne v] lines, it fails to reproduce the He II/Hβ ratio or its trend. These are the fatal diagrams for the classic U sequence and, at the same time, a vindication of the $A'_{m/i}$ sequence.

Finally, contrary to expectations, the UV data do not really provide significant additional input. This is not just because the data are too poor but because strong UV resonance lines are not unique to shock models: the thin component of the $A_{m/i}$ models also generates strong UV resonance lines. An exception is the N v λ1240 line, which *is* significantly stronger in shocks than in $A_{m/i}$ models. Although high N v/C IV ratios (>0.5) strongly implicate shocks (or very high U models), the converse, N v/C IV < 0.1, is quite normal for photoionization but unambiguously excludes shocks. Our own data on N v are inconclusive because of their low S/N, although there is some indication that shocks may make a contribution, at least to this line.

5.8. *Comparison with Other Studies*

Since the publication of photoionizing shock model grids by DS96, there have been many attempts to identify the dominant ionization mechanism in AGNs, particularly those with pronounced jets. Since Mrk 78 is perhaps the archetypal jet-dominated NLR, how do our results compare with other studies? Broadly speaking, they are consistent. Despite initial interest in the importance of shock-related ionization in Seyfert galaxies, most recent studies either find ambiguous evidence or a definite preference for photoionization, albeit including an optically thin component.

Perhaps least surprising are objects with clear conical or biconical emission regions: studies of NGC 5252 (Acosta-Pulido et al. 1996), NGC 5643 (Simpson et al. 1997; Evans et al. 1999), and NGC 5728 (Evans et al. 1999) all favor photoionization. An exception is NGC 2992, for which Allen et al. (1999) conclude that pre- plus postshock emission provides a better fit, although there are still significant difficulties with [O I], [O III] λ4363, [Ne v], and He II.[8]

[8] Note that in Figs. 18 and 20 in Allen et al. (1999) the shock trajectories are plotted $\sim$0.3 dex too low for He II λ4686/Hβ, and their correct placement strengthens their case for shocks.

Turning to Seyfert galaxies with a clearer association between radio and emission-line structures, Mrk 573 (Ferruit et al. 1999) and NGC 3393 (Cooke et al. 2000) have remarkable emission-line arcs that sheathe radio lobes. In both cases, however, there is no clear-cut signature of shock-related ionization, and both studies ultimately favor photoionization, although in the case of Mrk 573, the increase in required ionizing flux with radius prompts the suggestion that radiation from fast shocks provides the additional photoionizing source at larger radii (however, see § 7.2 below for an alternative possibility).

In the case of NGC 2110 and NGC 5929, Ferruit et al. (1999) placed FOS apertures on extranuclear emission-line knots likely to lie within the radio jet/outflow region. Despite a marginally better match to the shock models, the authors were unable to find a clear preference, in part because uncertain reddening undermined the usefulness of the UV observations.

Perhaps the most extreme examples of rapidly accelerated gas are the fast ($\sim$3200 km s^{-1}) filaments seen in NGC 1068 (Cecil et al. 2002). These filaments are thought to result from material ablated off higher mass clouds and rapidly accelerated, either radiatively or mechanically, up to a few thousand kilometers per second in only a few parsecs. Despite these extreme conditions, Cecil et al. argue that the clouds are photoionized by the central source rather than by shock-related processes.

Unfortunately, even when data are extensive and of high quality, ambiguities can remain. In the case of NGC 1068, for example, Capetti et al. (1997) and Axon et al. (1998) use WFPC2 and FOC images and spectra across the jet region to infer the importance of shock-related ionization. On the other hand, Kraemer et al. (1998) use FOS spectra of essentially the same regions and conclude that photoionization is dominant (although they do acknowledge the need for at least some additional heating given the high temperatures inferred by Kriss et al. 1992 from Hopkins Ultraviolet Telescope measurements of the C III] λ1909/C III λ977 and N III] λ1750/N III λ991 ratios). Similarly, in the case of NGC 4151, Winge et al. (1997) use FOC spectra to stress the importance of shock-related ionization, whereas Nelson et al. (2000) and Kraemer et al. (2000) use STIS spectra and conclude that photoionization dominates.

Given these prior results, what does our study of Mrk 78 contribute? First, the NLR velocity field of Mrk 78 is unambiguously dominated by jet-gas interactions (Papers I and III). Thus, Mrk 78 is one of the best candidates among Seyfert NLRs for identifying shock-related ionization. Second, unlike many of the other studies, we have enough spatial coverage to generate clear spatial trends in the line ratio diagrams, not just isolated points. These trends add great discriminating power and give confidence when rejecting some models and preferring others. Third, we have factored into the analysis the likely nuclear nitrogen overabundance and its effect on several of the diagrams. We suspect that in many previous studies, the [N II] line ratios (in particular [N II]/Hα) have been taken at face value and have therefore undermined confidence in any of the models because the [N II] diagrams required different parameters to fit the measurements. Fourth, we have not been content to adopt only those $A_{m/i}$ sequences available in the literature, which select specific ionization parameters and optical depths for the optically thick and thin components (optimized for the average Seyfert NLR). Instead, recognizing that the standard $A_{m/i}$ sequence of BWS96 overpredicts the high-ionization lines for Mrk 78, we searched for a better $A_{m/i}$ sequence ($A'_{m/i}$). Once again, the success of this sequence in essentially all the diagrams greatly strengthens our confidence in the relevance of this class of model.

Whereas previous studies using line ratio diagnostics have tended to find ambiguous or weak evidence favoring central source photoionization of optically thick and thin gas, our observations provide a strong and unambiguous preference for this scenario. Furthermore, in the specific case of Mrk 78, with its strong jet-driven gas dynamics, our conclusion that shock-related ionization is unimportant may have widespread relevance for the ionization mechanisms in the whole class of AGNs with jet-dominated emission-line regions.

6. LINE PROFILE DIAGNOSTICS

In § 5 we considered whether specific models could match *integrated* line flux ratios. Here we extend our approach to focus on a possible dependence of line ratio on *velocity*—i.e., we consider possible differences in line profiles.

In general, of course, one expects differences in profile shape whenever two or more regions of differing velocity fall within the same aperture and have different ionization conditions and/or different reddening. Although line profile differences in Seyfert galaxies have been discussed extensively in the past (e.g., Pelat et al. 1981; De Robertis & Osterbrock 1984; Filippenko & Halpern 1984; Whittle 1985c; Veilleux 1991b), it should be stressed that in almost all these studies the data were acquired using a single relatively large ($\sim$1″–4″) nuclear aperture, and the observed profile differences almost certainly reflect large-scale radial gradients in the velocity and ionization conditions. Our situation is quite different: our small off-nuclear apertures span a tiny fraction of the total region and should be insensitive to these large-scale gradients. To first order, then, we expect few if any profile differences. However, the ionization mechanisms currently under scrutiny raise an interesting additional possibility. Both the shock and $A_{m/i}$ models specifically invoke *two* ionization components (pre- and postshock gas; optically thin and thick gas). Since these components are roughly cospatial, then any velocity difference between them would result in significant profile differences. Do we expect such velocity differences? The answer is obviously "yes" for the shock models: the preshock gas is likely to have low velocity compared with the postshock gas. The answer for the $A_{m/i}$ models is less clear, but might well be "yes" if, for example, the optically thin gas is ablated and accelerated away from the optically thick material (as suggested by BWS96). The simpler single-component U models, on the other hand, are unlikely to show this effect.

Figures 7*a* and 7*b* illustrate the expected profile differences between a primary emission line (in our case, [O III] λ5007) and a comparison emission line for the shock and $A'_{m/i}$ models, respectively. For illustration purposes only, we choose an idealized (and exaggerated) velocity difference between the two components: a negative-velocity Gaussian (*left*) for the preshock (or optically thin) component and a positive-velocity Gaussian (*right*) for the postshock (or optically thick) component. The diagrams show a wide range in relative contribution of the two ionization components to the primary line (varying along the x-axis; *thin solid profile*) and for the comparison line (varying along the y-axis; *thick solid profile*). The diagonal dashed line shows the locus at which the primary and comparison lines have exactly the same profile shape (same relative contribution from each ionization component). Elsewhere, significant profile differences are apparent. Superposed on each diagram are the model sequences (Fig. 7*a*, shock; Fig. 7*b*, $A'_{m/i}$) in which the primary line is [O III] λ5007 and the

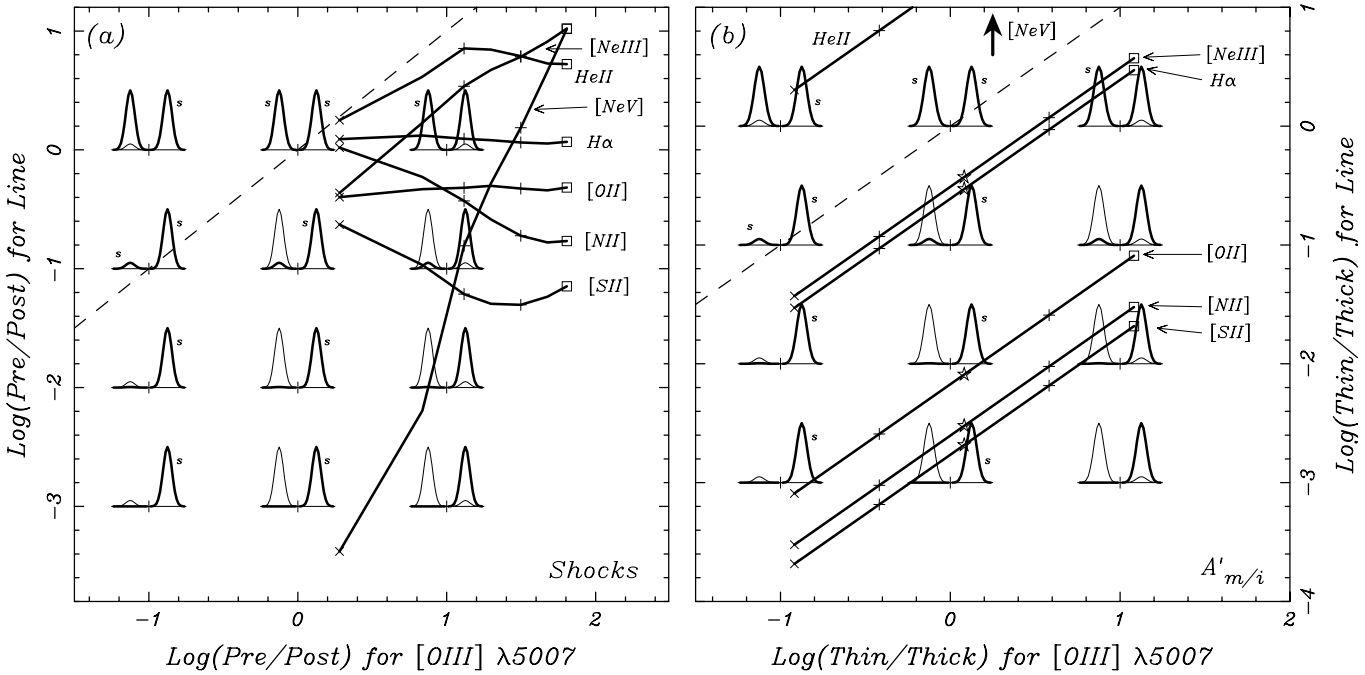

FIG. 7.—Profile comparisons for two-component models: (*a*) shocks, with pre- and postshock gas; (*b*) $A'_{m/i}$, with optically thin and thick gas. The plots cover a wide range in possible relative importance of each component for the [O III] λ5007 emission line (*x*-axis) and a comparison emission line (*y*-axis). To help illustrate profile differences, we assign the preshock/optically thin component to a blueshifted Gaussian and the postshock/optically thick component to a redshifted Gaussian. The resulting profiles are superposed as thin curves ([O III] λ5007) and thick curves (comparison line), and the dashed diagonal line shows the locus along which the two lines have identical profiles. Loci for shock (panel *a*) and $A'_{m/i}$ (panel *b*) model sequences are shown for [S II], [N II], [O II], [Ne III], [Ne V], He II, and Hα for the comparison line. On the loci, from the cross to the open square goes from low (200 km s^{-1}; $\log A'_{m/i} = -1.0$) to high (500 km s^{-1}; $\log A'_{m/i} = +1.0$), with plus signs for steps in shock velocity of 100 km s^{-1} and $A'_{m/i}$ of 0.5 dex. Both models predict significant profile differences for all lines. Note that for clarity, when the [O III] λ5007 and comparison components lie on top of each other, a small "s" ("similar") is plotted next to the component.

comparison lines are Hα, He II, [N II], [S II], [O II], [Ne III], and [Ne V] (note that [Ne V] lies off the plot in Fig. 7*b*).

The basic feature of these diagrams is that essentially all emission lines under all model conditions lie *away* from the diagonal dashed line; if the two ionization components have different velocity distributions, we should see strong profile differences between [O III] λ5007 and other emission lines. More specifically, for the shock models, if we demand the high ($\sim$500 km s^{-1}) shock velocities needed to best match the integrated line ratios, then the expected profile differences are at their *greatest*, especially for the low-ionization lines (Hα, [O II], [N II], and [S II]). For example, at 500 km s^{-1} [O III] λ5007 is strongly dominated by preshock emission ($\sim$99%), whereas [S II] is dominated by postshock emission ($\sim$90%). In these circumstances the [O III] and [S II] line profiles should come from completely different material, and even the slightest velocity difference between the pre- and postshock regions should be clearly noticeable. The situation for the $A'_{m/i}$ models is similar, only here the expected profile differences for the low-ionization lines are extreme throughout the entire $A'_{m/i}$ model range. Clearly, profile comparisons should give powerful insight into possible ionization mechanisms.

What do the data reveal? We find essentially *no* obvious profile differences, anywhere. More specifically, we explored two approaches, one simple but coarse, the other complex but more sensitive. As described in § 3.2, when measuring emission-line fluxes we used the [O III] λ5007 line as a template, shifting in velocity space to match the line to be measured. Throughout this procedure it was clear that the [O III] λ5007 profile provides an excellent fit in almost all circumstances (justifying this technique for measuring line fluxes). Figure 8 shows one example of the kind of profile match typical of our data: the [O III] profile from region LW-5 in slit A matches quite closely the Hα and [N II] profiles from the same region. In a more focused approach, we first excluded regions of lower S/N, as well as regions of steep flux and/or velocity gradients (where even small slit registration errors can lead to spurious profile differences). This restricted our analysis to LW-1, LW-2, LW-5, and LE-1 (note that LW-1 and LE-1 are sites of strong jet-gas interaction, and a detailed profile comparison at these locations should provide a sensitive probe of shock-ionized gas). Across these regions, the [O III] λ5007 line was fitted by one to four Gaussians, and this fit was compared with the other emission lines after first adjusting for differences in velocity and instrument resolution. To first order, the profiles were well matched. Occasionally, small adjustments to the amplitude of a Gaussian component improved the fit, suggesting minor variations in the ionization of the different Gaussian components, but nowhere were the Gaussians offset in velocity or had the wrong FWHM.

To second order, however, we could identify in many lines an additional weak broad feature of FWHM $\sim$ 700 km s^{-1} containing $\leq$10% of the total flux and being somewhat more prominent in the low-ionization lines. Villar-Martín et al. (1999) find a similar but stronger component in high-redshift radio galaxies. Although this is qualitatively consistent with a low-level contribution from high-velocity postshock gas, the weakness (and breadth) of the feature prevents us from making a more detailed statement.

In conclusion, we find that across the entire region, different emission lines have very similar profiles. If line-emitting gas is inherently divided into two different ionization components, then the velocity distributions of those two components must

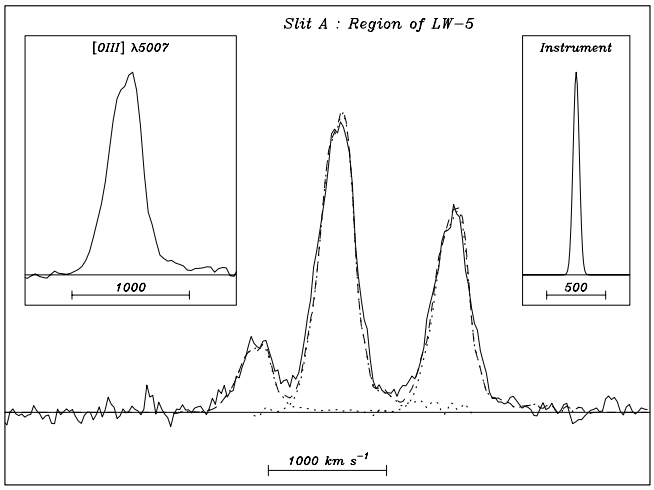

FIG. 8.—Example comparison between the [O III] λ5007 profile and the Hα and [N II] profiles from the LW-5 region of the western lobe in slit A. The [O III] profile is shown as an inset and as dotted lines (summed to give the dashed line) superposed on the Hα and [N II] profile. All plots have the same velocity scale, and the STIS instrumental profile is also shown.

be very similar. Under the shock paradigm this seems most unlikely; one expects significantly different velocity distributions for the pre- and postshock gas. Consequently, we regard our profile analysis as adding yet more evidence *against* photoionizing shocks as a major contributor to the line emission (although they may provide the weak, low-ionization, broad component noted above). Similarly, if there is a mixture of optically thin and thick photoionized material, then the velocity distributions of these two components must also be similar. Given the support for the $A'_{m/i}$ models from the integrated line ratio analysis, we regard this profile constraint as important: whatever process generates the optically thin and thick material, it cannot give rise to a significantly different velocity distribution for the two components. This argues against, for example, a scenario in which the optically thin material is stripped away from optically thick clouds and accelerated independently by a jet or wind.

7. LINE RATIOS VERSUS OTHER QUANTITIES

Sections 5 and 6 restricted their analysis to the emission lines themselves, comparing line and profile ratios directly with the various models. Although useful, this approach has its limitations, not least because the models have been developed and refined with the principal goal of matching these same line ratios. An alternative and potentially powerful approach is to look for correlations between line ratios and *other* properties of the region. Previous work of this type has tended to rely on single-aperture data for a sample of objects (e.g., Heckman et al. 1981; Dahari & De Robertis 1988; Veilleux 1991a; Whittle 1985b, 1992). Here, we have an unusual opportunity to explore such relations across a single dynamically active NLR. Two obvious lines of attack are to look for correlations between line ratios and gas kinematics (as expected, if shocks are dominant) or between line ratios and distance from the nucleus (as might be expected for central source photoionization). We now discuss each of these in turn.

7.1. *Gas Kinematics*

Measurements of kinematic parameters using the [O III] λ5007 line profile were described in § 3.4 (and will be discussed in more detail in Paper III). We consider three parameters: C80, the peak velocity (relative to systemic); FWHM; and QV_{sum}, the quadrature sum of the previous two. Apart from projection factors, these characterize, respectively, bulk velocity, velocity spread, and "total" velocity. No resolution corrections are needed for the STIS data, whereas the FOS data were corrected by subtracting the instrumental FWHM (320 km s^{-1}) in quadrature, assigning a lower limit of 150 km s^{-1} for apertures 1 and 9, in which the measured line width is comparable to the instrumental line width (see Paper I, § 5). Overall, these kinematic parameters all span a sufficiently large range ($\sim$100–1000 km s^{-1}) that trends with ionization should be readily seen. In Figures 9*a* and 9*b*, we show two examples of kinematic parameters plotted against excitation, with shock models (preshock plus postshock) superposed, with shock velocity assumed to match the corresponding kinematic parameter. Although it is unlikely that such a simple quantitative correspondence exists, there should be a general correspondence between measured velocity and shock velocity, and such plots help illustrate not only the predicted shock model line ratio but, more importantly, its variation with velocity.

There are two fairly clear *null results*. First, there are no strong correlations between any line ratios and any of the kinematic parameters. Second, the data show no connection to the shock models. In particular, although the line ratios remain relatively constant across a very wide range of velocities, the shock models instead predict strong trends with shock velocity. These results are found for all kinematic parameters and all line ratios.

In summary, there is no clear connection between the kinematics and the ionization state of the gas. Although shock models predict strong trends of line ratios with shock velocity, these trends are not seen in the data. Once again, the evidence weighs against shock ionization in Mrk 78 and, by extension, in other jet-dominated Seyfert galaxies.

7.2. *Aperture Location*

The obvious alternative to shock-related ionization is central source photoionization, and in this case we might expect correlations between line ratios and distance from the nucleus. Unfortunately, of course, other factors can undermine or add scatter to such correlations, including, for example, gradients and/or a local spread in gas density and/or optical depth. Despite these potential complexities, what do the data show?

For a wide range of line ratios we find a general decline in excitation with distance from the nucleus; Figure 9*c* shows one example: [O III]/[O II]. In general terms this is consistent with central source photoionization: at larger radii, the nuclear ionizing radiation field is diluted, and hence the ionization level drops.

Going beyond this simple inference, however, requires assumptions. Consider first a situation in which the standard U models apply: we have optically thick clouds of a single density at each location with a small total covering factor. In this case, the line ratio gradients suggest that U decreases roughly as r^{-1} (e.g., Fig. 9*c*, in which [O III]/[O II] $\approx 550U$ for a wide range of conditions; see Penston et al. 1990). Since $U \approx L_{ion}/4\pi r^2 c n_e$, our inferred U gradient of r^{-1} translates, roughly, to a density gradient of r^{-1}. Note that this gradient is *not* seen in our direct density estimates using the [S II] lines, which, at face value, yield $n_e \sim 10^2$–10^3 cm^{-3} everywhere. Unfortunately, it is not clear how to regard this difference, since there are reasons to doubt the applicability of the [S II] estimates: they are close to the low-density limit where errors are large, and in

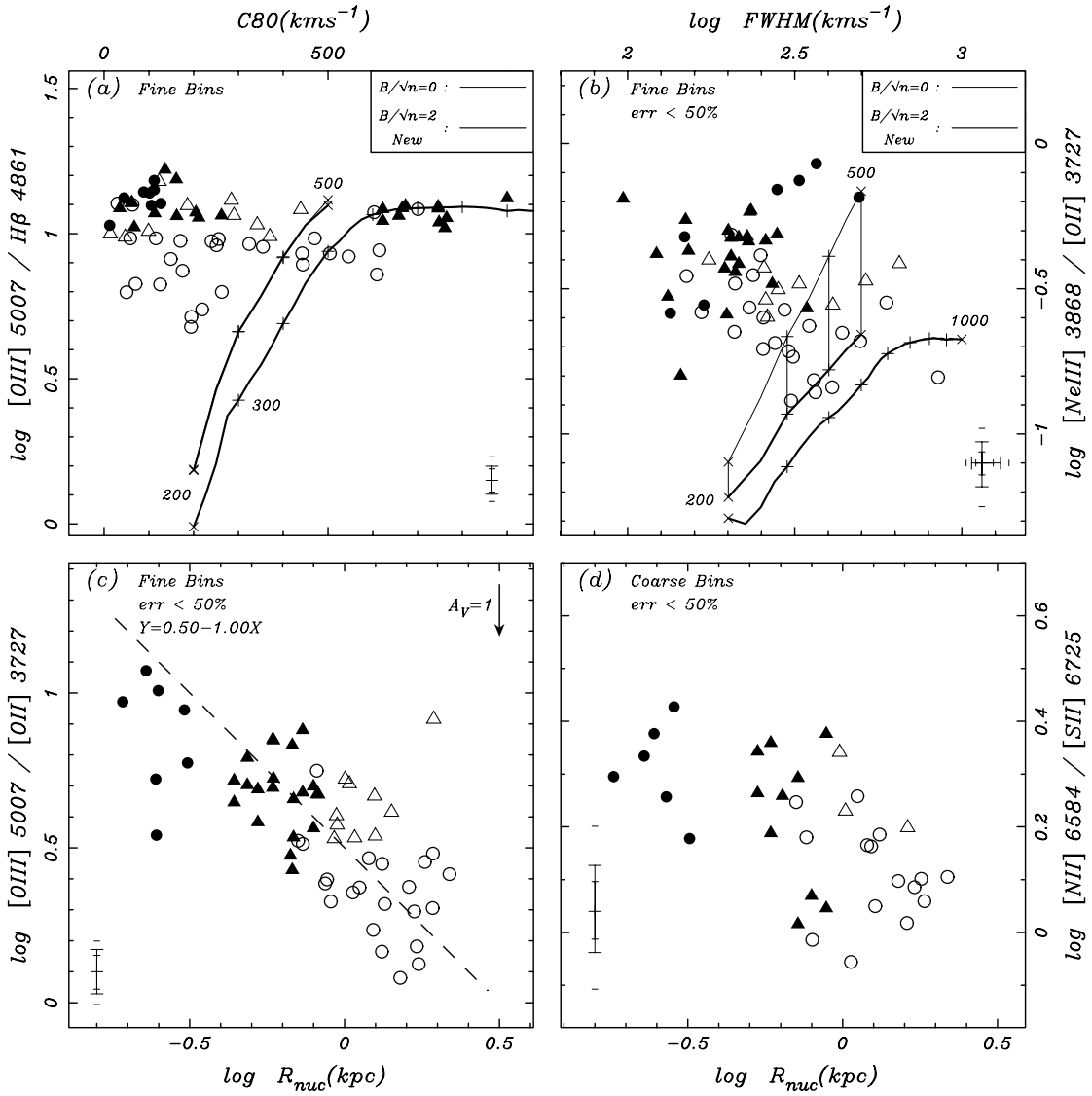

FIG. 9.—Line ratios vs. kinematic parameters and nuclear distance. Symbols, binning, reddening, and error bars are as described in Fig. 3. (*a*) Excitation vs. [O III] λ5007 profile peak velocity. (*b*) Excitation vs. [O III] FWHM. Superposed are three shock sequences: the magnetic and nonmagnetic sequences from DS95 and the new magnetic sequence from M. G. Allen (2004, private communication). The sequences are placed so that the kinematic parameter equals the shock velocity. Evidently, excitation is largely independent of local kinematics. (*c*) Excitation vs. radius. The dashed line is not a fit but a line of gradient −1. (*d*) The [N II] λ6584/[S II] ratio vs. radius. This ratio is essentially independent of excitation (see model trajectories on Fig. 4*d*), and the gradient instead shows an increased nuclear nitrogen abundance by about a factor of 2.

the presence of a range of densities, the [S II] lines tend to reflect the denser and/or optically thick material, whereas other lines may reflect the less dense and/or optically thin material.

These uncertainties bear directly on a long-standing issue in AGN nebular physics, namely, the so-called *Q* problem (e.g., Metz et al. 1997; Allen et al. 1999; Robinson et al. 2000). Mild or even zero excitation gradients are often found in the NLRs and ENLRs of Seyfert and radio galaxies. When these gradients are analyzed using standard *U* models and [S II] densities, one finds ionizing flux gradients that are *flatter* than r^{-2}, apparently inconsistent with simple geometric dilution of a central ionizing source. (Stated differently, the inferred ionizing photon output of the nucleus, $Q_{\rm ion}$, seems to increase with radius instead of remaining constant.) To date there is no clear resolution of this problem, although a number of suggestions have been made: projection effects undermine the simple analysis (e.g., Metz et al. 1997), additional in situ sources of ionization such as shocks add to the off-nuclear radiation field, [S II] ratios are unreliable measures of n_e (e.g., Allen et al. 1999), and radiation pressure alters cloud structure to modify its effective radiation parameter and [S II] density (Dopita et al. 2002).

Given the evidence in § 5 favoring the $A_{m/i}$ models over the $U_{1.4}$ and $U_{\rm dust}$ models, it is clearly important to reevaluate the *Q* problem within the framework of the two-component $A_{m/i}$ models. Although a thorough examination of this is beyond the scope of this paper, we make one or two brief comments. First, the extra degree of freedom introduced by having two components of different *U* prevents one inferring the ionizing flux from the observed line ratios using a single "effective *U*"; recall that although the optically thin and thick components have quite different *U*, they have different densities and can experience the similar ionizing flux at a given radius. Second, even if one could arrive at a credible effective *U* using

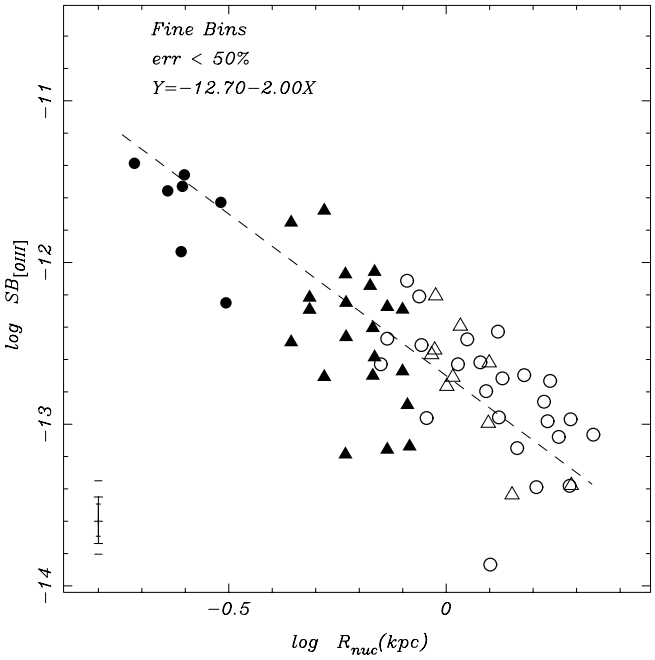

FIG. 10.—[O III] line surface brightness $SB_{[O\ III]}$ vs. radius in kiloparsecs. The units of $SB_{[O\ III]}$ are ergs s^{-1} cm^{-2} $arcsec^{-1}$. Symbols, binning, reddening, and the error bar are as described in Fig. 3. The dashed line is not a fit but a line of gradient −2.

integrated line ratios, inferring the all-important gas density using [S II] is problematic when two components are present; although most of the [S II] comes from the high-density optically thick component, the high-ionization lines (which help define U) come mainly from the low-density optically thin phase. One could imagine, for example, a situation in which the optically thin and thick components have different density gradients, which, even in the presence of an r^{-2} radiation field, could yield a classic Q problem. Given these uncertainties, we choose not to invoke the Q problem to constrain, one way or the other, the relative importance of an r^{-2} radiation field and/or the presence of off-nuclear sources of ionizing radiation. We simply note that the observed systematic decrease of excitation with increasing radius in Mrk 78 at least suggests the dominance of a global rather than local ionizing mechanism, in which case, AGN photoionization might be a more natural explanation than shock ionization.

Note that the two-component $A_{m/i}$ model has also been invoked to solve another problem: the [O III] temperature problem, in which typical [O III] λ4363/[O III] λ5007 ratios yield excessively high temperatures (∼20,000 K) compared with the predictions of standard U models (∼12,000 K) (Tadhunter et al. 1989). As noted in § 5.5, such high temperatures occur in the optically thin gas, and this emission dominates the integrated ratio. Here, we simply note that appealing to two-component models (such as $A_{m/i}$) may provide the needed solutions to both the [O III] temperature problem and the Q problem.

Finally, we consider the [O III] emission-line surface brightness, $SB_{[O\ III]}$. Figure 10 reveals the strongest correlation in our entire data set: $SB_{[O\ III]}$ drops systematically with projected nuclear distance, approximately as r^{-2}. To clarify the degree to which this is a fundamental correlation, we must consider other properties that also show radial gradients. For example, ionization degree drops, statistically, with radius (see above); perhaps the $SB_{[O\ III]}$ gradient is really following the ionization gradient, since there is evidence for a link between ionization and $SB_{[O\ III]}$ (e.g., Acosta-Pulido et al. 1996; Robinson et al. 1994). Performing a partial correlation, using $SB_{[O\ III]}$, [O III]/Hβ, and r, we do *not* recover the relation discussed by these authors and confirm the basic dependence of $SB_{[O\ III]}$ on radius. This correlation is at least consistent with nuclear photoionization, since ultimately line emission reflects reprocessed nuclear radiation, which itself drops with radius. Conversely, if shocks dominate the line emission, we would expect strong correlations between surface brightness and kinematic parameters, since line luminosity is a strong function of shock velocity. The fact that we find *no* such correlation argues against the importance of shock ionization.

8. NUCLEAR IONIZING LUMINOSITY

An important test of the viability of central source photoionization is to check whether there is basic consistency between the luminosity and ionization of the emission-line region and the luminosity and spectral shape of the central source. Of course, in the case of Mrk 78, the central source is hidden from view behind a dust lane, so we must make use of indirect methods to assess its properties. We have *two* indirect tracers of the nuclear luminosity: (1) the NLR ionization parameter, U, which is related to $Q_{\rm ion}$, the total nuclear production rate of ionizing photons, and (2) the reprocessed far-infrared (FIR) luminosity, $L_{\rm IR}$, which is related to the integrated nuclear output, $L_{\rm ph}$, at shorter wavelengths than a nominal dust absorption cutoff ($\lambda_{\rm low}$, which we take to be ∼4000 Å; see below). For central source photoionization our principal tracer for the nuclear luminosity is the Hβ luminosity. The test of central source photoionization is to ask whether the nuclear luminosities inferred from U and/or $L_{\rm IR}$ are consistent with those inferred from the Hβ luminosity.

Starting with a central isotropic power-law source with $L_\nu \propto \nu^{-\alpha_{\rm o}}$ ($\alpha_{\rm o} > 1.0$), we first give an expression for the ionizing photon production rate, $Q_{\rm ion}$, in terms of $L_{\rm ph}$, the integrated luminosity shortward of $\lambda_{\rm low}$ (in angstroms), and the energy per photon $\epsilon_{\rm H} = h\nu_{\rm Lyc}$ at the Lyman limit:

$$Q_{\rm ion} = \frac{\alpha_{\rm o} - 1}{\alpha_{\rm o}} \left(\frac{\lambda_{\rm low}}{912}\right)^{1-\alpha_{\rm o}} \frac{L_{\rm ph}}{\epsilon_{\rm H}}\ {\rm s}^{-1}. \quad (1)$$

If this source ionizes the surrounding gas, which has covering factor C_i, then, assuming most ionizing photons ionize hydrogen, we have two equivalent relations for the Hβ luminosity, one involving $Q_{\rm ion}$ and the other involving $L_{\rm ph}$:

$$L_{\rm H\beta} = C_i Q_{\rm ion} \frac{\alpha_{\rm H\beta}}{\alpha_B} \epsilon_{\rm H\beta} \approx (4.78 \times 10^{-13}) C_i Q_{\rm ion}\ {\rm ergs\ s}^{-1}, \quad (2)$$

$$L_{\rm H\beta} \approx C_i L_{\rm ph} \frac{\alpha_{\rm H\beta}}{\alpha_B} \frac{\epsilon_{\rm H\beta}}{\epsilon_{\rm H}} \frac{\alpha_{\rm o} - 1}{\alpha_{\rm o}} \left(\frac{912}{\lambda_{\rm low}}\right)^{\alpha_{\rm o}-1} \approx 0.023 C_i L_{\rm ph} \frac{\alpha_{\rm o} - 1}{\alpha_{\rm o}} \left(\frac{912}{\lambda_{\rm low}}\right)^{\alpha_{\rm o}-1}\ {\rm ergs\ s}^{-1}, \quad (3)$$

where $\alpha_{\rm H\beta}$ and α_B are the Hβ and total case B recombination coefficients for hydrogen at $T = 10^4$ K and $\epsilon_{\rm H\beta} = h\nu_{\rm H\beta}$ is the energy per Hβ photon.

Since for Mrk 78 $L_{\rm H\beta} = 1.4 \times 10^{42}$ ergs s^{-1} (uncorrected for reddening), then basic consistency with central source photoionization requires $\log(C_i Q_{\rm ion}) \sim 54.5$ and $\log(C_i L_{\rm ph}) \sim 44.6$ (taking $\alpha_{\rm o} = 1.4$ and $\lambda_{\rm low} \sim 4000$ Å). What do the data suggest

for $Q_{\rm ion}$ and $L_{\rm ph}$, and do the values support central source photoionization?

8.1. $Q_{\rm ion}$ *from* U

A classic derivation of $Q_{\rm ion}$ uses the distance from the nucleus, D, electron density, n_e, and ionization parameter, U, via the well-known relation

$$Q_{\rm ion} = 4\pi D^2 n_e c U \ {\rm s}^{-1} = (8.40\times10^{49})\theta^2\left(\frac{cz}{H_0}\right)^2 n_e U \ {\rm s}^{-1}, \quad (4)$$

where θ is the angular distance from the nucleus in arcseconds and H_0 is the Hubble constant. Recalling our discussion from § 7.2, it is unclear what values to choose for n_e and U, since the [S II] estimates may be biased to high values, and the preference for $A_{m/i}$ models undermines a simple estimate of U from line ratios. With these caveats in mind, we consider two approaches.

First, consider at face value the [S II] density estimates and the use of the simple $U_{1.4}$ sequence. With $H_0 = 75$ km s^{-1} Mpc^{-1} and $\theta \sim 1''$, we have $\log U \sim -2.2$ and $\log n_e \sim 3$, giving $\log Q_{\rm ion} \sim 55.0$, which would agree with our predicted value if $C_i \sim 0.3$. Given the considerable uncertainties of these estimates, this must be considered as a good match and supports the basic nuclear photoionization scenario.

It is unclear how to extend this analysis to the $A_{m/i}$ models, since they are evaluated using a single ionizing flux and two different densities to achieve a spread in U. Taking these models at face value (see § 4.2), we have $\log U = -1.8$ and $\log n_e = 1.7$ for the optically thin gas and $\log U = -3.3$ and $\log n_e = 3.4$ for the optically thick gas. Again, choosing $1''$ for a characteristic distance, we have $\log Q_{\rm ion} \sim 54.3$, again consistent with the observed Hβ luminosity and a modest covering factor.

Despite the uncertainties surrounding the choice of n_e and U in equation (4), our values are unlikely to be wildly inaccurate, and hence we regard the close match to the observed Hβ luminosity with a modest and plausible NLR covering factor as strong support for the dominance of the central source photoionization scenario.

8.2. $L_{\rm ph}$ *from* $L_{\rm IR}$

It is well known that much of an AGN's central optical–UV–X-ray output is absorbed by dust and ultimately reradiated in the infrared (e.g., Rieke 1978; Pérez-García & Rodríguez-Espinosa 2001). Thus, as long as other IR sources are secondary, $L_{\rm IR}$ can act as a bolometer for the AGN, modulo the dust covering factor, C_d. One might argue that $C_d \sim 1 - C_i$, since the radiation that does not ionize the gas gets blocked by the dusty material. However, that is probably an underestimate, since much of the emitted line radiation is itself absorbed by dust and contributes to $L_{\rm IR}$, suggesting that $C_d \sim 1$ would be a reasonable approximation. Under these circumstances, we have $L_{\rm IR} \approx L_{\rm ph}$, and we can use equation (3) directly to estimate $L_{\rm H\beta}$.

From Sanders & Mirabel (1996) we have, for a distance d measured in centimeters,

$$L_{\rm IR} \approx (1.8\times10^{-11})4\pi d^2 \times (13.5S_{12} + 5.2S_{25} + 2.58S_{60} + S_{100}) \ {\rm ergs \ s^{-1}}, \quad (5)$$

where for Mrk 78, $S_{12} = 0.13$, $S_{25} = 0.55$, $S_{60} = 1.11$, and $S_{100} = 1.13$ are the four *IRAS* 12–100 μm fluxes, in janskys, from which we obtain $\log L_{\rm IR} \sim 44.60$. Using equation (3), with $\alpha_{\rm o} = 1.4$ and $\lambda_{\rm low} \sim 4000$ Å, we find agreement with the observed Hβ luminosity as long as $C_i \approx 1.0$. Once again, within the considerable uncertainties, we consider this as significant support for the importance of central source photoionization.

It is still important, however, to check that the IR luminosity in Mrk 78 is indeed dominated by reprocessed AGN light, given possible additional contributions from star formation and diffuse "cirrus." There are several approaches to this. First, Mrk 78 has both "warmer" FIR colors and a significant FIR excess compared with normal galaxies. Using the H-band flux from the Two Micron All Sky Survey to characterize the underlying starlight and the definition of $L_{\rm FIR}/L_H$ from Sanders & Mirabel (1996), we find values of $L_{\rm FIR}/L_H \sim 6$ for Mrk 78, compared with only ~0.1 for a typical Sb galaxy (Kennicutt 1998), confirming Mrk 78 to have a strong FIR excess by a factor of ~60. Similarly, adopting the FIR spectral shape parameters from Miley et al. (1985), we find $\alpha(60, 25) = -0.79$ and $\alpha(100, 60) = -0.03$ (where α here follows the convention $f_\nu \sim \nu^\alpha$)—significantly warmer than normal galaxies and all but the most extreme starburst galaxies. Could the FIR emission originate in an extreme starburst, perhaps hidden behind the dust lane? Almost certainly not. First, both our own data and the spectral synthesis work of Cid Fernandes et al. (2001), González Delgado et al. (2001), and Raimann et al. (2003) all show Mrk 78 to have a central population comprising a mixture of old (≥5 Gyr) and intermediate-age (a few hundred megayears) stars, with no evidence of a current starburst. Second, applying starburst FIR conversion factors from Kennicutt (1998) to our observed FIR luminosity, we expect a star formation rate of ~20 $M_\odot$ yr^{-1} with associated Hα luminosity $\sim 4.5\times10^{42}$ ergs s^{-1}. This is comparable to the *entire* observed Hα luminosity. Given that nowhere within the NLR, including the nuclear dust lane, do our line ratios or profile comparisons show a low-excitation (starburst) contribution at even the ~10% level, we feel we can strongly rule out such a component.

We conclude that despite our inability to see the central UV source directly, both NLR and FIR emission reveal its luminosity in a consistent manner, reinforcing our earlier conclusion that the NLR is indeed photoionized by the central AGN.

9. RECENT X-RAY SPECTROSCOPY RESULTS

We end this paper by noting some recent results that focus on similar issues but with a completely different approach: that of high-resolution X-ray spectroscopy (see, e.g., Paerels & Kahn 2003). *XMM-Newton* and *Chandra* observations of Seyfert 2 galaxies, of which the most impressive example is NGC 1068 (e.g., Kinkhabwala et al. 2002), show spectra that are rich in radiative recombination features from highly ionized species (C VI, C V, N VII, N VI, O VIII, and O VII, for example). The critical fact is that radiative recombination *continua*, located at the ionization threshold, are *narrow*, only a few electron volts wide. Clearly, the recombining electron population is *cool* (~several times 10^4 K) compared with a thermal X-ray–emitting gas. This is conclusive evidence that the high-ionization gas is photoionized by a hard spectrum and not collisionally ionized by shocks. In this context, NGC 1068 has similar status to Mrk 78: it has broad forbidden lines that are clearly accelerated by radio-emitting ejecta. This failure to find X-ray shock signatures in NGC 1068, like our failure to find optical shock signatures in Mrk 78, together make a strong case against significant shock ionization in these and related AGNs.

10. SUMMARY AND CONCLUSION

We have made a detailed study of the ionization conditions in the jet-disturbed NLR of Mrk 78, aiming to identify the dominant ionization mechanisms with particular emphasis on establishing whether or not shock-related ionization is important.

To quantify the various mechanisms, we rely on three widely studied models: AGN photoionization of optically thick gas ($U_{1.4}$ sequence), AGN photoionization of optically thick and thin gas ($A_{m/i}$ sequence), and fast shocks, and one new class of model: AGN photoionization of dusty, radiation pressure–dominated gas ($U_{\rm dust}$ sequence). Our approach includes the use of line ratio-ratio diagrams, a comparison of line profiles, a search for correlations between line ratios and other properties, and the use of surrogate measures of the hidden AGN luminosity. Gratifyingly, all these approaches yield a consistent picture, one in which shock ionization plays at most a minor role, in which central source photoionization dominates throughout the region, and in which a range of optical depths seems likely.

Empirically, our ratio-ratio analysis follows a standard route, with minor modifications. As we introduce successive classes of line ratio, a consistent picture emerges: all models match the simplest excitation ratios (e.g., [O III]/Hβ vs. [O III]/[O II]), ratios that separate out shocks consistently favor photoionization (e.g., [O III]/Hβ vs. [S II]/Hα), and ratios that separate all three consistently favor $A_{m/i}$ models over $U_{1.4}$, $U_{\rm dust}$, and shock models (e.g., [Ne III]/[O II] vs. [Ne V]/[Ne III]). We provide some details as follows. (1) Mrk 78 has lower overall excitation than the average Seyfert 2 galaxy, forcing us to evaluate an optimized $A'_{m/i}$ sequence with lowered optically thin ionization parameter. (2) The NLR is sufficiently well sampled that we find trends in the ratio plots, and these trends almost always follow the $A'_{m/i}$ model sequences. (3) All ratios that include [N II] λ6584 are systematically enhanced at smaller radii, pointing to an enhanced nitrogen abundance in the circumnuclear regions by roughly 2 times. (4) Allowing for this, all ratio plots yield consistent values of $A'_{m/i}$ spanning $-0.5 < \log A'_{m/i} < +1.0$ (and, for the most part, $U_{1.4}$ spanning $-3.0 < \log U < -2.0$). (5) The UV line ratios do not discriminate between shock and photoionization models, although it is suggested that the N V λ1240 line could play such a role. (6) Shocks and $U_{\rm dust}$ models systematically overpredict [O I] λ6300, but we choose to downplay this line, since it is difficult to model in all four scenarios. (7) The $U_{\rm dust}$ models overpredict [Ne III], He II, and [S II], but more importantly, their trend with excitation, a hallmark of these models, is opposite to the observed trends for both He II and [S II].

Given our aim of elucidating the role of shocks, it is natural to introduce kinematics into the study, which we do in two ways. First, we find that at every location different emission lines have roughly the same profile shape. Since both the shock and $A_{m/i}$ models each include two components with quite different spectra (pre- and postshock; optically thin and thick), then the two components must share similar velocity distributions. Although this can be considered as an interesting constraint for the $A_{m/i}$ scenario, it brings fairly strong evidence *against* the shock scenario, since it seems most unlikely that the pre- and postshock have the same velocity. Second, we find essentially no correlation between any line ratio and any kinematic parameter; the slowest and the fastest gas have essentially the same spectra. Needless to say, the shock models predict extremely strong correlations between shock velocity and line ratios, so we take this as further evidence against the importance of shock ionization. Nevertheless, we do find some evidence for a weak, broad, low-ionization component consistent with a minor ($\leq$10%) postshock component.

The strongest correlation we find is between excitation and distance from the nucleus. Qualitatively, at least, this supports central source photoionization. As with many AGNs, however, when we use standard U models and [S II] densities to evaluate the dependence of ionizing flux on radius, we find a gradient *flatter* than r^{-2}, inconsistent with simple central source illumination; in other words, Mrk 78 exhibits the classic Q problem. We speculate, without detailed justification, that the resolution to the Q problem might lie with the $A_{m/i}$ scenario, since simple estimates of U and density that assume a single gaseous component are clearly misleading when, in fact, both optically thick and optically thin gas are present.

Finally, we find strong support for central source photoionization by performing a simple luminosity analysis. Using the ionization conditions in the NLR and, independently, the total FIR luminosity, we estimate the luminosity of the (hidden) nuclear ionizing source. These estimates are not only consistent with each other but, more importantly, with the total Hβ luminosity of the NLR, assuming central source photoionization and a total NLR covering factor in the plausible range $\sim$20%–100%.

In conclusion, our analysis strongly supports the dominance of central source photoionization and argues against the importance of shock-related ionization. Since the NLR of Mrk 78 is dominated by hydrodynamic acceleration, our negative result for shock ionization is important and calls into question the role of shocks in ionizing the gas in other AGNs. We also find problems with the simplest picture, in which the NLR contains only optically thick gas. By introducing a range of optical depths, the $A_{m/i}$ models are more successful and provide a plausible refinement of the original picture. Ultimately, if multiple components exist, they cannot have significantly different velocity, since the line profiles of different species are, to first order, so similar. This places an important constraint on the interconnection, direct or indirect, between gas acceleration and gas ionization.

It is a pleasure to thank Mike Dopita, Ralph Sutherland, Brent Groves, Luc Binette, and Clive Tadhunter for stimulating and helpful discussions. We also thank Rosa González Delgado for providing the stellar template spectra and Mark Allen for versions of the updated shock models. D. J. R. and M. W. thank Inter-University Center for Astronomy and Astrophysics, Mount Stromlo Observatory, and the University of New South Wales for hospitality while some of this work was completed. Support for proposals GO5417, GO7404, and GO8459 was provided by NASA through a grant from the Space Telescope Science Institute, which is operated by the Association of Universities for Research in Astronomy, Inc., under NASA contract NAS5-26555.

REFERENCES

Acosta-Pulido, J. A., Vila-Vilaró, B., Pérez-Fournon, I., Wilson, A. S., & Tsvetanov, Z. I. 1996, ApJ, 464, 177
Aldrovandi, S. M. V., & Contini, M. 1984, A&A, 140, 368
———. 1985, A&A, 149, 109
Allen, M. G., Dopita, M. A., & Tsvetanov, Z. I. 1998, ApJ, 493, 571
Allen, M. G., Dopita, M. A., Tsvetanov, Z. I., & Sutherland, R. S. 1999, ApJ, 511, 686
Axon, D. J., Marconi, A., Capetti, A., Macchetto, F. D., Schreier, E., & Robinson, A. 1998, ApJ, 496, L75
Baldwin, J. A., Phillips, M. M., & Terlevich, R. 1981, PASP, 93, 5

Binette, L., Wilson, A. S., & Storchi-Bergmann, T. 1996, A&A, 312, 365 (BWS96)
Capetti, A., Axon, D. J., & Macchetto, F. D. 1997, ApJ, 487, 560
Cardelli, J. A., Clayton, G. C., & Mathis, J. S. 1989, ApJ, 345, 245
Cecil, G., Dopita, M. A., Groves, B., Wilson, A. S., Ferruit, P., Pécontal, E., & Binette, L. 2002, ApJ, 568, 627
Cid Fernandes, R., Heckman, T. M., Schmitt, H., González Delgado, R. M., & Storchi-Bergmann, T. 2001, ApJ, 558, 81
Clark, N. E., Axon, D. J., Tadhunter, C. N., Robinson, A., & O'Brien, P. 1998, ApJ, 494, 546
Cooke, A. J., Baldwin, J. A., Ferland, G. J., Netzer, H., & Wilson, A. S. 2000, ApJS, 129, 517
Dahari, O., & De Robertis, M. M. 1988, ApJS, 67, 249
Davidson, D., & Netzer, H. 1979, Rev. Mod. Phys., 51, 715
De Robertis, M. M., & Osterbrock, D. E. 1984, ApJ, 286, 171
Dopita, M. A., Groves, B. A., Sutherland, R. S., Binette, L., & Cecil, G. 2002, ApJ, 572, 753
Dopita, M. A., & Sutherland, R. S. 1995, ApJ, 455, 468 (DS95)
———. 1996, ApJS, 102, 161 (DS96)
———. 2003, Astrophysics of the Diffuse Universe (Berlin: Springer)
Evans, I., Koratkar, A., Allen, M. G., Dopita, M. A., & Tsvetanov, Z. I. 1999, ApJ, 521, 531
Ferland, G. J. 1996, Hazy: A Brief Introduction to CLOUDY (Univ. Kentucky Dep. Phys. Astron. Internal Rep.) (Lexington: Univ. Kentucky)
Ferland, G. J., & Mushotsky, R. F. 1984, ApJ, 286, 42
Ferland, G. J., & Netzer, H. 1983, ApJ, 264, 105
Ferruit, P., Wilson, A. S., Falcke, H., Simpson, C., Pécontal, E., & Durret, F. 1999, MNRAS, 309, 1
Filippenko, A. V., & Halpern, J. P. 1984, ApJ, 285, 458
Fosbury, R. A. E., Mebold, U., Goss, W. M., & Dopita, M. A. 1978, MNRAS, 183, 549
Gaskell, C. M., & Ferland, G. J. 1984, PASP, 96, 393
González Delgado, R. M., Leitherer, C., & Heckman, T. M. 2001, ApJ, 546, 845
Groves, B. A., Dopita, M. A., & Sutherland, R. S. 2004a, ApJS, 153, 9 (GDS04a)
———. 2004b, ApJS, 153, 75 (GDS04b)
Halpern, J. P., & Steiner, J. E. 1983, ApJ, 269, L37
Heckman, T. M. 1980, A&A, 87, 152
Heckman, T. M., Miley, G. K., van Breugel, W. J. M., & Butcher, H. R. 1981, ApJ, 247, 403
Jacoby, G. H., Hunter, D. A., & Christian, C. A. 1984, ApJS, 56, 257
Keel, W. C., & Miller, J. S. 1983, ApJ, 266, L89
Kennicutt, R. C., Jr. 1998, ARA&A, 36, 189
Kimble, R. A., et al. 1998, ApJ, 492, L83
Kinkhabwala, A., Sako, M., Behar, E., Kahn, S. M., Paerels, F., & Brinkman, A. C. 2002, ApJ, 575, 732
Kraemer, S. B., Crenshaw, D. M., Hutchins, J. B., Gull, T. R., Kaiser, M. E., Nelson, C. H., & Weistrop, D. 2000, ApJ, 531, 278
Kraemer, S. B., Ruiz, J. R., & Crenshaw, D. M. 1998, ApJ, 508, 232
Kriss, G. A., Davidsen, A. F., Blair, W. P., Ferguson, H. C., & Long, K. S. 1992, ApJ, 394, L37
Leitherer, C., et al. 1999, ApJS, 123, 3
Metz, S. K., Tadhunter, C. N., Robinson, A., & Axon, D. J. 1997, in ASP Conf. Ser. 113, Emission Lines in Active Galaxies: New Methods and Techniques, ed. B. M. Peterson, F.-Z. Cheng, & A. S. Wilson (San Francisco: ASP), 390
Miley, G. K., Neugebauer, G., & Soifer, B. T. 1985, ApJ, 293, L11
Morse, J. A., Raymond, J. C., & Wilson, A. S. 1996, PASP, 108, 426
Nelson, C. H., Weistrop, D., Hutchings, J. B., Crenshaw, D. M., Gull, T. R., Kaiser, M. E., Kraemer, S. B., & Lindler, D. 2000, ApJ, 531, 257
Paerels, F. B. S., & Kahn, S. M. 2003, ARA&A, 41, 291
Pagel, B. E., & Edmunds, M. G. 1981, ARA&A, 19, 77
Pelat, D., Alloin, D., & Fosbury, R. A. E. 1981, MNRAS, 195, 787
Penston, M. V., et al. 1990, A&A, 236, 53
Pérez-García, A. M., & Rodríguez-Espinosa, J. M. 2001, ApJ, 557, 39
Raimann, D., Storchi-Bergmann, T., González Delgado, R. M., Cid Fernandes, R., Heckman, T. M., Leitherer, C., & Schmitt, H. 2003, MNRAS, 339, 772
Rieke, G. H. 1978, ApJ, 226, 550
Robinson, A., et al. 1994, A&A, 291, 351
Robinson, T. G., Tadhunter, C. N., Axon, D. J., & Robinson, A. 2000, MNRAS, 317, 922
Sanders, D. B., & Mirabel, I. F. 1996, ARA&A, 34, 749
Shuder, J. M. 1981, ApJ, 244, 12
Simpson, C., Wilson, A. S., Bower, G., Heckman, T. M., Krolik, J. H., & Miley, G. K. 1997, ApJ, 474, 121
Stasinska, G. 1984, A&A, 135, 341
Storchi-Bergmann, T., Rodriguez-Ardila, A., Schmitt, H. R., Wilson, A. S., & Baldwin, G. A. 1996a, ApJ, 472, 83
Storchi-Bergmann, T., Wilson, A. S., Mulchaey, J. S., & Binette, L. 1996b, A&A, 312, 357
Sutherland, R. S., Bicknell, G. V., & Dopita, M. A. 1993, ApJ, 414, 510
Tadhunter, C. N., Robinson, A., & Morganti, R. 1989, in Extranuclear Activity in Galaxies, ed. E. J. A. Meurs & R. A. E. Fosbury (Garching: ESO), 293
Unger, S. W., Pedlar, A., Axon, D. J., Whittle, M., Meurs, E. J. A., & Ward, M. J. 1987, MNRAS, 228, 671
Veilleux, S. 1991a, ApJS, 75, 383
———. 1991b, ApJ, 369, 331
Veilleux, S., & Osterbrock, D. E. 1987, ApJS, 63, 295
Viegas, S. M., & Gruenwald, R. B. 1988, ApJ, 324, 683
Viegas-Aldrovandi, S. M., & Contini, M. 1989a, ApJ, 339, 689
———. 1989b, A&A, 215, 253
Villar-Martín, M., Binette, L., & Fosbury, R. A. E. 1996, A&A, 312, 751
Villar-Martín, M., Tadhunter, C. N., Morganti, R., Axon, D., & Koekemoer, A. 1999, MNRAS, 307, 24
Whittle, M. 1985a, MNRAS, 213, 1
———. 1985b, MNRAS, 213, 33
———. 1985c, MNRAS, 216, 817
———. 1992, ApJ, 387, 121
Whittle, M., Pedlar, A., Meurs, E. J. A., Unger, S. W., Axon, D. J., & Ward, M. J. 1988, ApJ, 326, 125
Whittle, M., Silverman, J. D., Rosario, D. J., Nelson, C. H., & Wilson, A. S. 2004, AJ, submitted (Paper III)
Whittle, M., & Wilson, A. S. 2004, AJ, 127, 606 (Paper I)
Wilson, A. S., & Willis, A. G. 1980, ApJ, 240, 429
Winge, C., Axon, D. J., Macchetto, F. D., & Capetti, A. 1997, ApJ, 487, L121
Woodgate, B. E., et al. 1998, PASP, 110, 1183
Yee, H. K. C. 1980, ApJ, 241, 894